Title

High-Speed, Multi-Modal Diffuse Optical Spectroscopic Imaging for Translational Biophotonics

Author

Lam, Jesse Hou

Publication Date

2020

UNIVERSITY OF CALIFORNIA,
IRVINE

High-Speed, Multi-Modal Diffuse Optical Spectroscopic Imaging for Translational Biophotonics

DISSERTATION

submitted in partial satisfaction of the requirements for the degree of

DOCTOR OF PHILOSOPHY

in Biomedical Engineering

by

Jesse Hou Lam

Dissertation Committee:
Professor Bruce J. Tromberg, Chair
Professor Anthony J. Durkin
Professor Michael Green

2020

TABLE OF CONTENTS

LIST OF FIGURES AND TABLES

LIST OF SYMBOLS

μ_a	Absorption coefficient
μ_s	Scattering coefficient
μ'_s	Reduced scattering coefficient
T	Transmission
L	Photon pathlength
I	Detected photon intensity
I_0	Initial photon intensity
ε	Molar extinction coefficient
C	Molar concentration
g	Anisotropy
θ	Angle of scattering
λ	Wavelength of light
a	Reference scattering value for the scattering power law
b	Scattering power
A	Absorbance
c_0	Speed of light in a vacuum
c	Speed of light in tissue
n_{tissue}	Index of refraction of tissue
u	Radiance term from the Boltzmann Transport Equation (BTE)
$\mathbf{r}$	Position term in the BTE
$\mathbf{\Omega}$	Direction term in the BTE
$\mathbf{t}$	Time term in the BTE
q	Source term in the BTE
p	Phase term in the BTE
U	Integral of radiance with respect to all solid angles in the BTE
S	Isotropic source term in the BTE
D	Diffusion constant

ω	Modulation frequency
i	Complex number
P	Optical power
A	Amplitude of modulation
δ	Dirac function
τ	Absorption relaxation time
α	Factor to relate relative blood flow to absolute blood flow
β	Arterial blood fraction
ρ_8	Source-detector separation of 8 mm
ρ_{10}	Source-detector separation of 10 mm
ρ_{16}	Source-detector separation of 16 mm
ρ_{20}	Source-detector separation of 20 mm
ρ_{24}	Source-detector separation of 24 mm
p	Statistical significance

ACKNOWLEDGEMENTS

To Kelsey, to Cris and Pete, to all of my friends and family, thank you for supporting me through this difficult, yet exhilarating time in my life.

To the DOSI lab, despite recent hardships, I can't help but feel like we've grown a lot closer. In particular, Tim Quang and Brian Hill have helped me tremendously throughout my PhD expedition. Whether it be editing, data collection, or debugging, Tim and Brian have always offered a helping hand without question. If I could nominate "co-first authors" for this dissertation, it would be them. To Amanda Durkin, Hossein Yazdi, Rob Warren, and the rest of the DOSI lab members, even when you were incredibly busy, you always made time for me, thank you!

To Albert Cerussi, who inspired me to dive headfirst into the world of diffuse optics, you've made joining DOSI lab one of the best decisions of my life. To Tom O'Sullivan and of course Bruce Tromberg, both who guided me through this journey, I could not have asked for better mentors. To Sehwan "Paul" Kim and Seonguk "Joe" Cho who taught me so much about the collaborative spirit, the meaning of hospitality, and Korean culture, I will remember my visits to Cheonan for the rest of my life.

To all of the Beckman Laser Institute, this has honestly been the most intellectually stimulating 4 years of my life. There was never a time where I felt limited during my pursuit of knowledge. BLI is a place like no other, every single person I've met here has been so kind and enthusiastic. Thank you to everyone for being who they are!

Finally, I gratefully acknowledge my funding sources: Air Force Office of Scientific Research (FA9550-14-1-0034 and FA9550-17-1-0193), the Leading Foreign Research Institute Recruitment Program through the National Research Foundation of Korea funded by the Ministry of Science and ICT (NRF-2018K1A4A3A02060572), the Laser Microbeam and Medical Program, and the Arnold and Mabel Beckman Foundation

CURRICULUM VITAE

Jesse H. Lam

EDUCATION

UNIVERSITY OF CALIFORNIA, IRVINE

PhD | Biomedical Engineering | Expected: DEC 2019

Advisor: Dr. Bruce J. Tromberg

MSc | Biomedical Engineering | MAY 2018

BSc | Biomedical Engineering | Biophotonics Specialization | JUN 2014

SKILLS

OPTICAL | Lasers, photodiodes, spectrometers, and tissue-simulating phantoms

ELECTRICAL | Breadboarding, soldering, and surface-mount technology

MECHANICAL | Mills, lathes, band saws, power tools, and 3-D printers

SOFTWARE | MATLAB, SolidWorks, ExpressPCB, and Microsoft Windows

RESEARCH EXPERIENCE

PHD CANDIDATE | SEPT 2015 – DEC 2019

***Department of Biomedical Engineering**, University of California, Irvine*

- Analyzed biomedical signals in MATLAB to estimate the metabolism of a human hand using pulsatile hemodynamics as a surrogate for blood flow
- Prototyped a motion-tracked probe to image tissue hemoglobin over 100 cm^2 of tissue at millimeter resolution while reducing the scanning time from 30 minutes to 5 minutes
- Investigated a method to track catheter needle position for direct drug delivery to a nerve plexus using a combined ultrasound and photonics approach

JUNIOR SPECIALIST | JUN 2014 – SEPT 2015

***Beckman Laser Institute and Medical Clinic**, University of California, Irvine*

- Collaborated with the U.S. Army Institute of Surgical Research to analyze hemorrhage and resuscitation hemodynamic signals of 10 swine publishing findings in *Military Medicine*
- Optically characterized tissue-simulating silicone phantoms to mimic a tumor inside breast tissue in order to optimize tissue spectroscopic devices

UNDERGRADUATE RESEARCHER | AUGUST 2013 – JUNE 2014

***Beckman Laser Institute and Medical Clinic**, University of California, Irvine*

- Designed fiber-based flexible probes for the measurement of muscles during stationary exercise routines such as treadmills
- Designed and machined a custom probe compatible with 12 mm laparoscopic trocars to measure *in-vivo* the physiological composition of swine kidney capsules

TEACHING EXPERIENCE

TEACHING ASSISTANT | FALL 2015 | WINTER 2016 | FALL 2016 | WINTER 2017 | WINTER 2018

***Department of Biomedical Engineering**, University of California, Irvine*

- Formulated new labs from the ground-up to instruct 66 graduate and undergraduate students how to assemble and calibrate a grating-based benchtop spectrometer
- Coordinated with multiple teaching assistants and 2 professors to distribute homework creation and grading duties
- Held weekly review and discussion sessions for 224 Biomedical engineering students resulting in an average approval rating of 3.8/4.0 based on quarterly evaluations

PUBLICATIONS

IN PREPARATION

Jesse H. Lam, Brian Hill, Robert Amelard, Sehwan Kim, Seonguk Cho, Timothy Quang, Hossein S. Yazdi, Robert V. Warren, Kyle B. Cutler, and Bruce J. Tromberg, "Multi-modal diffuse optical spectroscopy for high-speed monitoring and wide-area mapping of tissue optical properties and hemodynamics."

Hossein S. Yazdi, George P. Philipopoulos, **Jesse Lam**, Brian Hill, Bruce J. Tromberg, "Multimodal Diffuse Optical Spectroscopies for real time subsurface imaging of tissue composition, metabolism, and vascular dynamics."

PUBLISHED

Robert Amelard, **Jesse H Lam**, Brian Hill, Amanda Durkin, Kyle Cutler, Bruce J Tromberg, "Monocular 3D Probe Tracking for Generating Sub-Surface Optical Property Maps from Diffuse Optical Spectroscopic Imaging," *IEEE Transactions on Biomedical Engineering,* October 2019 (in pre-print).

Jesse H Lam, Thomas D O'Sullivan, Tim S Park, Jae H Choi, Robert V Warren, Wen-Pin Chen, Christine E McLaren, Leopoldo C Cancio, Andriy I Batchinsky, Bruce J Tromberg, "Non-invasive Dual-Channel Broadband Diffuse Optical Spectroscopy of Massive Hemorrhage and Resuscitative Endovascular Balloon Occlusion of the Aorta (REBOA) in Swine," *Military Medicine*, 183(suppl_1), August 2018, pp. 150-156.

Jessica P Miller, Dolonchampa Maji, **Jesse Lam**, Bruce J Tromberg, Samuel Achilefu, "Noninvasive depth estimation using tissue optical properties and a dual-wavelength fluorescent molecular probe in vivo," *Biomedical Optics Express*, 8(6), June 2017, pp. 3095-3109.

Hossein S Yazdi, Thomas D O'Sullivan, Anais Leproux, Brian Hill, Amanda Durkin, Seraphim Telep, **Jesse Lam**, Siavash S Yazdi, Alice M Police, Robert M Carroll, Freddie J Combs, Tomas Strömberg, Arjun G Yodh, Bruce J Tromberg, "Mapping breast cancer blood flow index, composition, and metabolism in a human subject using combined diffuse optical spectroscopic imaging and diffuse correlation spectroscopy," *Journal of biomedical optics*, 22(4), April 2017.

Albert E. Cerussi, Kevin Conde, **Jesse Lam**, and Vaibhav Verma "Broadband characterization of tissue simulating phantoms using a supercontinuum laser in a scanning diffuse optical spectroscopy instrument", *Proc. SPIE 9319*, Optical Tomography and Spectroscopy of Tissue XI, March 2015, pp. 93191Z.

PATENT APPLICATIONS

S Yazdi, B Tromberg, M Green, T Quang, **J Lam**, T O'Sullivan, A Cerussi, "Gigahertz Bandwidth ASIC for Time-Resolved Frequency Domain Optical Metrology," US 62/868,592.

BJ Tromberg, **J Lam**, T Quang, "Optical subsurface object localization using temporally-resolved photon density waves," US 62/694,689.

Abstract of the Dissertation

High-Speed, Multi-Modal Diffuse Optical Spectroscopic Imaging for Translational Biophotonics
By
Jesse Hou Lam
Doctor of Philosophy in Biomedical Engineering
University of California, Irvine, 2019
Professor Bruce J. Tromberg, Chair

Diffuse optical spectroscopic imaging (DOSI) is a non-invasive and quantitative technique to recover absolute tissue optical properties and chromophores. Over the past decade, our DOSI device has been utilized as a "one size fits all" standard bedside instrument to serve all of our research needs. In breast cancer research, we have screened dozens of patients studying the spectral profile of tumors and monitoring their response to chemotherapy. In military medicine, the same DOSI technology has been used to investigate hemorrhagic shock and novel resuscitative techniques. However, recent applications have revealed limitations of our DOSI device, requiring more capabilities than what is currently offered. In breast cancer research, more modalities are needed in order to effectively screen patients, such as a continuous imaging mode to locate contrast and generate chromophore maps, as well as a dual-channel mode to perform analysis on layered tissue. In military medicine, there is a need for a high-speed and more portable system to capture hemodynamics and metabolism of traumatically injured patients.

To meet the needs of these applications, I present advances in DOSI technology. A broadband-capable, high speed DOSI has been demonstrated on tissue-simulating optical phantoms where a buried object was successfully imaged using a continuous scan over a wide area. Separation of layers in a heterogenous phantom was also presented wherein a subsurface object was invisible from the point of view of a shallow probe, but detectable using a sufficiently deep measurement. In addition, sensitivity to layers of tissue was verified on a human participant wherein adipose and underlying muscle tissue were shown to have different deoxygenation rates under the condition of a short arterial occlusion. The metabolic rate of oxygen consumption of human thenar tissue was estimated using pulsatile hemoglobin signals captured by DOSI. Benefits of a two-channel DOSI instrument was demonstrated in a study of massive hemorrhage and resuscitative endovascular balloon occlusion of the aorta. Finally, I propose the future direction of DOSI with preliminary work developing a portable DOSI device.

CHAPTER 1: Introduction

1.1 Motivation for a high-speed, multi-modal tissue spectroscopy device

Bevilacqua et al. pioneered a method which combined frequency-domain photon migration (FDPM) and white-light continuous-wave near-infrared spectroscopy (CW-NIRS)[1]. This innovation expanded the capabilities of diffuse optical spectroscopic imaging (DOSI) systems by allowing greater access to both known and unknown tissue components. Rather than being limited to a few wavelengths as in FDPM systems, broadband DOSI allowed for the capture of absorption and scattering coefficients throughout the entire near-infrared (NIR) spectrum. As illustrated by figure 1, primary tissue chromophores oxy-hemoglobin (HbO2), deoxy-hemoglobin (HbR), lipid (FAT), and water (H2O) in the NIR contains non-flat features.

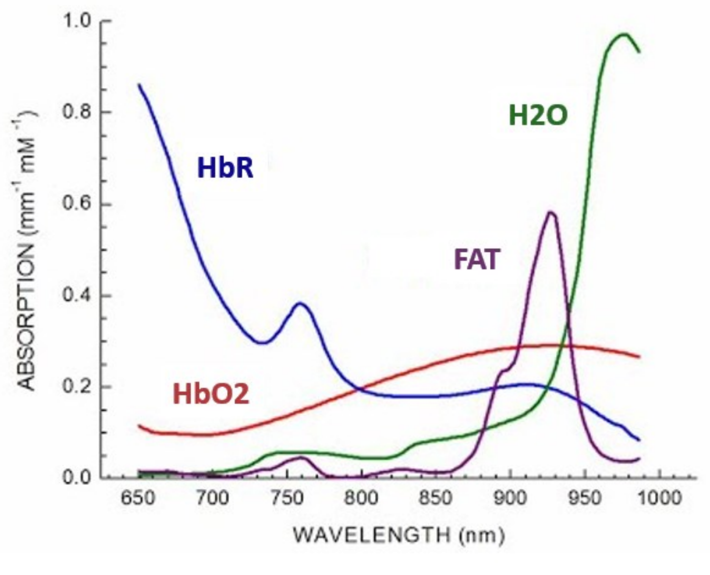

Figure 1: Extinction coefficients of primary tissue chromophore in the NIR.

Depending on the wavelength, certain laser diodes can be more or less sensitive to certain chromophores. For example, pulse-oximeters often choose sources with center wavelengths at 660 nm and 940 nm in order to probe HbR and HbO2, respectively[2,3]. However, with the introduction of broadband DOS, coverage of the absorption (μ_a) and reduced scattering (μ_s') throughout the NIR spectrum was comprehensive, providing greater freedom to select laser diode wavelengths. This allowed for optimization of DOSI devices, by selecting wavelengths which provide better signal-to-noise (SNR) as well as miniaturization of DOSI devices[4,5] as only a handful of laser diodes were now required. In addition, full-spectrum analysis belonging to unaccounted chromophores was now possible[6], such as the "specific tumor components" shown in figure 2.

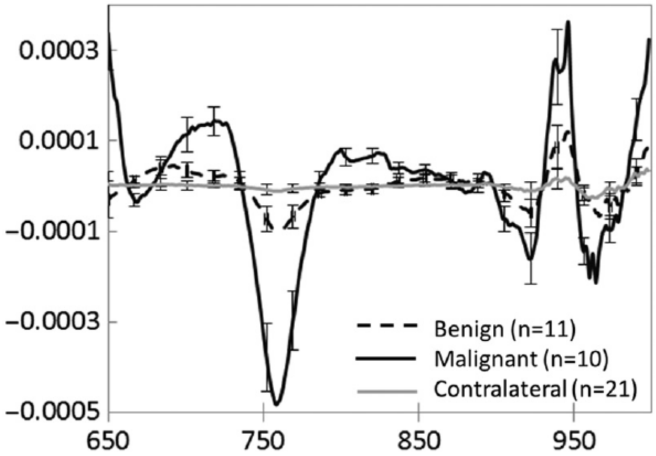

Figure 2: Differential diagnosis method to identify unique spectral features of benign versus malignant breast lesions enabled by using broadband DOSI[6]. After fitting the absorption spectrum with known chromophores, the residual absorption spectrum are the unknown components in the tissue.

However, our DOSI device has been utilized as a "one size fits all" standard bedside instrument to serve all of our research needs. In breast cancer research, we have screened dozens of patients studying the spectral profile of tumors and monitoring their response to chemotherapy. In military medicine, the same DOSI technology has been used to investigate hemorrhagic shock and novel resuscitative techniques. However, recent applications have revealed limitations of our DOSI device, requiring more capabilities than what is currently offered. In breast cancer research, more modalities are needed in order to effectively screen patients, such as a continuous imaging mode to locate contrast and generate chromophore maps, as well as a dual-channel mode to perform analysis on layered tissue. In military medicine, there is a need for a high-speed and more portable system to capture hemodynamics and metabolism of traumatically injured patients. Nearly two decades later, while DOSI had garnered reputation as a valuable clinical tool, the fundamentals of the instrument as a modality remained largely unchanged.

This dissertation describes the next technical achievement transforming DOSI into a flexible, multi-modal tissue spectroscopic device. While current MDOSI models only support full-spectrum broadband mode and low-resolution (centimeter-scale) spatial imaging, the newly developed DOSI includes modalities: 1) full-spectrum broadband mode, 2) high-resolution (millimeter-scale) spatial imaging mode, 3) dual-channel temporal measurement mode, and 4) high-speed pulsatile hemodynamic mode. advances in DOSI technology. To validate the next generation of multi-modal DOSI devices, I measured tissue-simulating optical phantoms where a buried object was successfully imaged using a continuous scan over a wide area. I show separation of layers in a heterogenous phantom wherein a subsurface object was invisible from the point of view of a shallow probe, but detectable using a sufficiently deep measurement. In addition, I verify sensitivity to layers of tissue on a human participant wherein adipose and underlying muscle tissue were shown to have different deoxygenation rates under the condition of a short arterial occlusion. I estimate the metabolic rate of oxygen consumption of human thenar tissue using pulsatile hemoglobin signals captured by DOSI. I demonstrate the benefits of having a multi-channel DOSI instrument in a study of massive hemorrhage and resuscitative endovascular balloon occlusion of the aorta. Finally, I propose the future direction of DOSI with preliminary work developing a portable DOSI device.

1.2 Fundamentals of Diffuse Optical Spectroscopic Imaging

DOSI instruments at the Beckman Laser Institute and Medical Clinic (BLIMC) represent a combination of multiple modalities, each with their own iterative improvements from over decades of research and development. This chapter will summarize some fundamental concepts of diffuse optics utilized by our DOSI devices at the BLIMC.

1.2.1 Low intensity light-tissue interactions in the near-infrared

When light interacts with tissue, many physical interactions will occur which may absorb or scatter the light. Low-intensity (tens of milliwatts), light-tissue interactions in the NIR are depicted in figure 3.

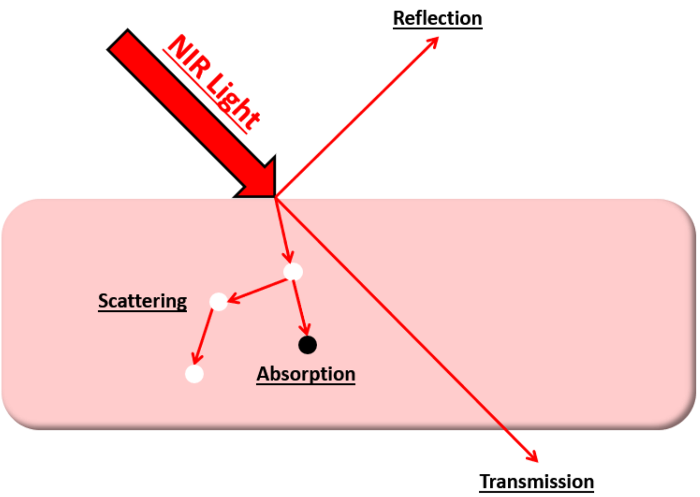

Figure 3: Light-tissue interactions relevant for DOSI measurements when using low intensity, NIR light. Scatterers are illustrated as white objects, while absorbers are shown as black objects.

Absorption

Absorption occurs when the energy of incident electromagnetic radiation matches the band gap of an electron in an atom, promoting the electron to a higher energy state. When the electron returns to its ground state, the absorbed energy is converted into vibrational modes (negligible heating). Other interactions such as auto-fluorescence and ablation are not relevant for typical DOSI applications. Appreciable autofluorescence of biological tissue utilizes wavelengths of light shorter than the NIR, while ablation requires high-intensity or short-pulsed lasers. A molecule containing atoms that absorb light, otherwise known as the chromophore of that molecule, can absorb light at a range of wavelengths. Mapping the absorption as a function of wavelength results in that chromophore's absorption spectrum. Absorption is denoted as μ_a with units mm^{-1} which describes the number of absorption events a photon will encounter per unit distance. The reciprocal of μ_a is known as the "mean free path", the average distance (total path length) a photon will travel before encountering an absorption event in a medium. μ_a is defined[7] as:

$$\mu_a = -\frac{1}{T}\frac{\partial T}{\partial L} \qquad [1]$$

Where L is the pathlength of light (e.g. length of a cuvette), and T is the transmitted fraction of light defined as:

$$T = \left(\frac{I}{I_0}\right) = 10^{-\varepsilon C L} \qquad [2]$$

With ε as the molar extinction coefficient, C as the concentration, L as the pathlength of light, I is the detected light intensity, and I_0 is the source light intensity. Solving for μ_a becomes much more complicated in tissue, due to the presence of scattering events which modify the pathlength of light.

The primary chromophores of the human body in the NIR are: oxyhemoglobin (HbO2), deoxyhemoglobin (HbR), water (H2O), and lipid (FAT). Interrogating deep (centimeter scale) into biological tissue is possible using what is known as the "optical window," a wavelength band in the NIR spanning ~650-1000 nm in which the overall absorption of the 4 prior mentioned chromophores is minimal. This allows for relatively deep photon penetration depth. Figure 4 displays the absorption spectrum of NIR chromophores for a simulated tissue (21 μM HbO2, 9 μM HbR, 40% H2O, 50% FAT).

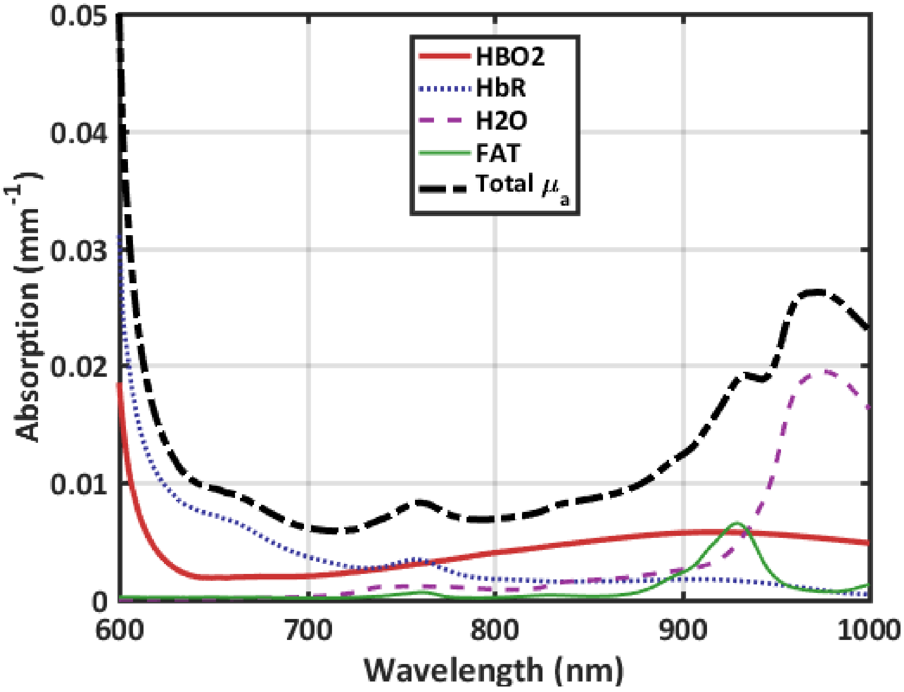

Figure 4: A simulated tissue (21 µM HbO2, 9 µM HbR, 40% H2O, 50% FAT) showing the absorption spectrum and the NIR optical window. The band of minimal absorption is found in the ~650-850 nm wavelength range.

Further analysis of the absorption spectrum reveals the lowest total absorption can be found in the ~650-850 nm band. The total absorption is the linear combination of chromophore absorption values.

Scattering

Scattering in tissue occurs because of changes in index of refraction, each scattering event changes the direction of the propagating photon. The directionality of scattering is represented by anisotropy, g:

$$g = cos\theta \qquad [3]$$

Anisotropy describes the degree (θ) of forward directionality after a scattering event. The value of g ranges from -1 to 1, where $g = -1$ would be a reflective interaction, $g = 0$ would be an isotropic scatter, and $g = 1$ would be transmission. g is typically estimated to be ~0.7-0.9 for biological tissue[7,8]. Multiple scattering events eventually causes injected photons (e.g. using an optical fiber) to lose its directionality, and thus become "diffuse". Two types of scattering are considered: Mie and Rayleigh. The method of scattering depends on the size of the particle interacting with the photons. For particles with a diameter significantly smaller than the wavelength of incident light, Rayleigh scattering is dominant. In the NIR, where micron-sized cells and organelles are comparable or larger than the wavelength of incident light, Mie scattering dominates[9]. Figure 5 shows a depiction of typical scattering sources in biological tissue.

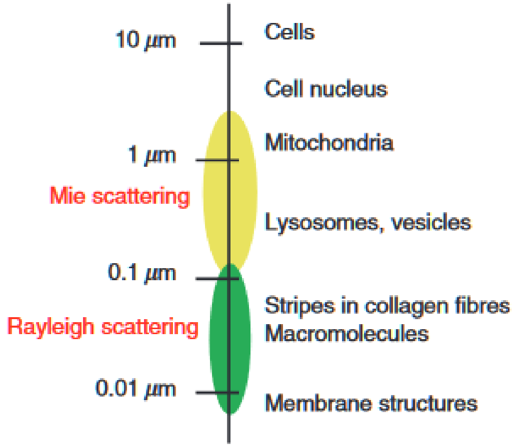

Figure 5: Example of scattering sources in biological tissue. In the NIR regime, Mie scattering is dominant[9].

Scattering is expressed as μ_s with units mm^{-1}. However, in the diffusive regime, where $\mu_s >> \mu_a$, it is preferable to work with the reduced scattering coefficient (μ_s') defined as:

$$\mu_s' = \mu_s(1 - g) \qquad [4]$$

μ_s' can be described as the scattering for an isotropic (non-directional) step. Similar to μ_a, $\frac{1}{\mu s'}$ describes the average distance between isotropic scattering events. Mie scattering in tissue can be modeled as a power-law function of wavelength[7,10,11] mathematically expressed as:

$$\mu_s'(\lambda) = a\left(\frac{\lambda}{500\ nm}\right)^{-b} \qquad [5]$$

a is the reference reduced scattering value defined as $[a = \mu_s'(500\ nm)]$ while λ is the wavelength in nanometers. b is the scattering power, and determines the degree of non-linearity over wavelength. This relationship between μ_s' and wavelength is exceptionally useful in diffuse optics as it allows for interpolation and extrapolation of scattering based on a few sample wavelengths.

Transmission and reflection

Transmission is not a substantial factor provided sufficiently thick samples wherein any exiting photons would not have had any appreciable effect on the detected signal. In other words, there is no practical difference between transmitted photons, and photons which are not picked up by the detector as a result of attenuation (scattering and absorption events).

On the other hand, some degree of surface reflection is unavoidable and is considered. It is assumed that any non-detected, reflected photons do not re-enter the medium given a source and detector sitting on the surface of a medium (e.g. a semi-infinite model)[12]. This assumption is valid by using infinitely absorbing material such as black polyoxymethylene (Delrin®) at the surface of the medium. Reflection effects are further mitigated by calibration to an optical material with a similar index of refraction as the medium.

The "cuvette problem" in DOSI

Given a transparent cuvette filled with an absorbing species as in figure 6, one can solve for the concentration in the cuvette by using equation [2]. For multiple absorbers in the same cuvette, one can simply solve for each species by a set of linear equations using Beer-Lambert Law:

$$A = L \sum_{i=1}^{N} \varepsilon_i C_i \qquad [6]$$

In this case, A is the sum of absorbances [$A = log_{10}\left(\frac{I}{I_0}\right)$], L is the length of the cuvette, ε_i is the molar extinction coefficient for each absorbing species in the cuvette, and C_i is the concentration of each absorber in the cuvette.

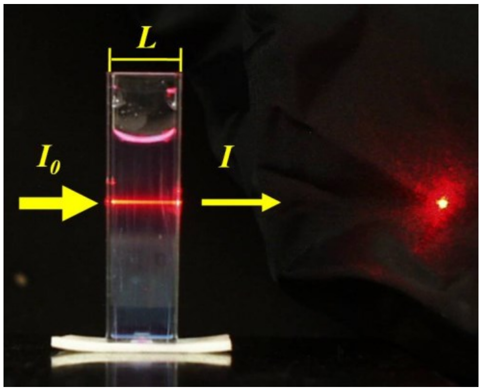

Figure 6: A transparent cuvette with an absorber and no scatterer.

However, Beer-Lambert law cannot be so simply applied when a scatterer is introduced, as depicted in figure 7. Due to scattering, the parameter describing the photon pathlength, *L*, is no longer defined as the length of the cuvette.

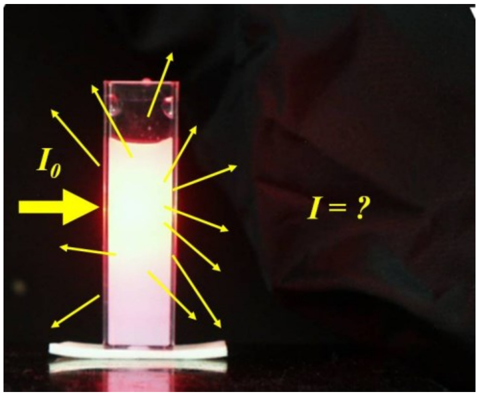

Figure 7: A turbid cuvette with a scattering agent. Note how the photon pathlength is no longer the length of the cuvette, as the light has transformed from a straight beam to a diffusive cloud.

While virtually impossible to physically measure pathlengths of individual propagating photons, one can instead use a model-based approach to mathematically estimate the degree of photon scattering.

1.2.2 Frequency-domain photon migration

One method to resolve μ_a from μ'_s is by utilizing FDPM which is based on diffusion theory[13–15] using a modulated light source. In the context of FDPM, photons can be described as two general behavior schemes: ballistic and diffusive. Ballistic photons are assumed to have some directionality. For example, a collimated beam of light will maintain directionality through a transparent medium (e.g. figure 4). For diffusive photons, a random walk is assumed where photon paths are scrambled by scattering events (e.g. figure 5). In tissue, it is assumed that scattering is the dominant interaction ($\mu'_s >> \mu_a$) for diffusion theory to accurately model photon propagation[16]. For ballistic photons, a Monte Carlo approach can be utilized. Although it will not be extensively covered in detail, the basic concept behind Monte Carlo simulation of photon propagation is to calculate the traversal of thousands to millions of photons in a medium based on absorption and scattering probabilities[17,18]. While a Monte Carlo approach is technically the most accurate method for modeling photons in turbid media, it is also the most computationally expensive. In contrast, some approximations of the diffusion equations can be performed in real-time, provided initial conditions are met with reasonable accuracy compared to Monte Carlo predictions, as shown in figure 8.

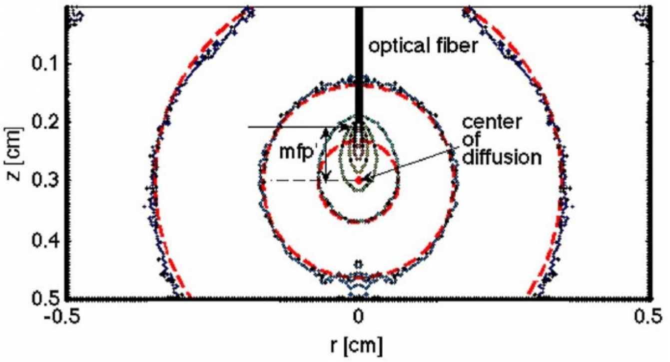

Figure 8: Comparison of photon propagation launched from a collimated beam as predicted by Monte Carlo (black) and diffusion theory (red). Outside of the diffusive regime, where photons have maintained some directionality, the diffusion equation fails to accurately account for photon propagation. However, once the light has sufficiently scattered, the diffusion equation provides an approximation of photon transport with comparable accuracy to Monte Carlo[16].

The Diffusion Equation

For a method to model light propagation, one starting point is the Boltzmann Transport Equation (BTE). The BTE can be written as[19,20] :

$$\frac{1}{\boldsymbol{c}}\frac{\partial u(\boldsymbol{r},\boldsymbol{\Omega},\boldsymbol{t})}{\partial \boldsymbol{t}} + \Omega\nabla \mathrm{u}(\mathbf{r},\boldsymbol{\Omega},\mathbf{t}) = -\mathrm{u}(\mathbf{r},\boldsymbol{\Omega},\mathbf{t})(\mu_a + \mu_s) + \mu_s \int\int_{4\pi} u(\boldsymbol{r},\boldsymbol{\Omega},\mathbf{t})\mathrm{p}(\boldsymbol{\Omega}\cdot\boldsymbol{\Omega})\, d\boldsymbol{\Omega} + q(\boldsymbol{r},\boldsymbol{\Omega},\mathbf{t}) \qquad [7]$$

Where $\boldsymbol{c}$ is the speed of light in a vacuum (c_0) normalized to the index of refraction of the medium (i.e. $c = \frac{c_0}{n_{tissue}}$) and $\mathrm{u}(\mathbf{r},\boldsymbol{\Omega},\mathbf{t})$ is the radiance at position $\mathbf{r}$, direction $\boldsymbol{\Omega}$, and at time $\mathbf{t}$. $\mathrm{p}(\boldsymbol{\Omega}\cdot\boldsymbol{\Omega})$ is the phase function, which accounts for photon scattering events projecting in direction $\boldsymbol{\Omega}$, and $q(\mathbf{r},\boldsymbol{\Omega},\mathbf{t})$ is the source term.

Several assumptions can be made to adapt the BTE into an equation which better describes diffusion. Firstly, isotropy of photon movement is assumed. That is, photon propagation has no preferential direction. Mathematically, this means integration over all solid angles ($d\boldsymbol{\Omega}$). The result is removal of dependence of [7] on direction $\boldsymbol{\Omega}$, with $\int\int_{4\pi} \mathrm{p}(\boldsymbol{\Omega} \cdot \boldsymbol{\Omega}) \cdot d\boldsymbol{\Omega} = 1$, as all photon scattering events will now be considered, rather than just in direction $d\boldsymbol{\Omega}$. Secondly, it is assumed that scattering events far outnumber absorption events, meaning $\mu_s \gg \mu_a$ or $\frac{\mu_s}{\mu_s+\mu_a} \sim 1$. The resulting photon diffusion equation is expressed as[20] :

$$\frac{dU(\boldsymbol{r},\boldsymbol{t})}{dt} = -c\mu_a U(\boldsymbol{r},\boldsymbol{t}) + S(\boldsymbol{r},\boldsymbol{t}) \pm D\nabla^2 U(\boldsymbol{r},\boldsymbol{t}) \qquad [8]$$

Where $U(\boldsymbol{r},\boldsymbol{t}) = \int\int_{4\pi} \mathrm{u}(\mathbf{r},\boldsymbol{\Omega},\mathbf{t})\, d\Omega$ and $S(\boldsymbol{r},\boldsymbol{t}) = \int\int_{4\pi} \mathrm{q}(\mathbf{r},\boldsymbol{\Omega},\mathbf{t}) d\Omega$. More specifically, $c \cdot \mu_a \cdot U(\boldsymbol{r},\boldsymbol{t})$ describes loss due to absorption and $S(\boldsymbol{r},\boldsymbol{t})$ describes the isotropic source when $\mu_s \gg \mu_a$. $D\nabla^2 U(\boldsymbol{r},\boldsymbol{t})$ may be positive or negative, depending on diffusion the position and time in the medium. Finally, D is the diffusion constant, defined as:

$$D = \frac{c}{3(\mu_a+\mu_s')} \sim \frac{c}{3\mu_s'} \qquad [9]$$

FDPM with Semi-Infinite Boundary Conditions

An "infinite" geometry[21,22] refers to a conceptual volume which is infinitely expansive in all directions in relation to the source and detector positions. This is useful in biomedical optics, particularly in simulations, as it means every single photon from a source in infinite media is accounted for by intra-medium interactions (e.g. absorption and scattering). In application, this environment can be approximated by placing a source-detection pair (e.g. extended via optical fibers) in the center of a very large container filled with some scattering and absorbing agents. However, for clinical usage, infinite medium geometries are rarely achieved as it requires insertion of the source and detection optical fibers into the tissue. To perform non-invasive DOSI measurements, a different type of geometry must be considered.

A "semi-infinite" geometry[22,23] refers to another conceptual volume, this time with a source-detector pair placed *on top* of an infinitely expansive medium. In practice, many tissue sites on the human body (e.g. breast, abdomen, calf, etc.) can be considered semi-infinite, even though in reality they are only a few centimeters wide and deep. As explained in the 1.2.1, this is because of detector limits – a detection scheme cannot differentiate signals from photons which escape the medium, and signals attenuated below the sensitivity of the detector.

FDPM utilizes a modulated light source, typically an NIR laser diode. This source can generally be defined as[23] :

$$U(\boldsymbol{r},\boldsymbol{t}) = U_{DC}(\boldsymbol{r}) + U_{AC}(\boldsymbol{r})e^{-i\omega t} \qquad [10]$$

Where $U(\boldsymbol{r},\boldsymbol{t})$ is the energy density, $U_{DC}(\boldsymbol{r})$ is referred to as the "direct-current," or average energy density, and $U_{AC}(\boldsymbol{r})e^{-i\omega t}$ is the modulated energy density at the modulation frequency (ω). This is known as a photon density wave[22]. If we define an amplitude modulated source as[23] :

$$s(\boldsymbol{r},\boldsymbol{t}) = Real\{P_{DC}\left(1 + Ae^{-i\omega t}\right)\}\delta(\boldsymbol{r}) \qquad [11]$$

Where P_{DC} is the average optical power and A is the amplitude modulation. From here, [10] and [11] can be inserted into the time-dependent diffusion equation [8]:

$$[D\nabla^2 U_{AC}(r) + i\omega U_{AC}(r) - \mu_a c U_{AC}(r) = -AP_{DC}\delta(r)]e^{-i\omega t} \qquad [12]$$

The solution to [12] can be drawn paralleling the solution using a DC source, resulting in[23]:

$$U_{AC}(r)e^{-i\omega t} = A \cdot P_{DC} \cdot \frac{1}{4\pi D}\frac{e^{-k_{real}r}e^{-i(k_{imag}r-\omega t)}}{r} \qquad [13]$$

Where $k_{real} = \sqrt{\frac{3}{2}\mu_a\mu_s'\sqrt{1+(\omega\tau)^2}+1}$, $k_{imag} = \sqrt{\frac{3}{2}\mu_a\mu_s'\sqrt{1+(\omega\tau)^2}-1}$, and τ is the absorption relaxation time.

1.2.3 Quantitative broadband DOSI

One limitation of FDPM is the reliance on discrete laser diodes. Incorporating more wavelengths allows for a higher confidence of fit when solving for chromophores, however, additional laser diodes add to the overall cost and size. Bevilacqua et al.

resolved this hurdle by combining white light spectroscopy with FDPM in order to extend the wavelength coverage to the entire NIR regime[1].

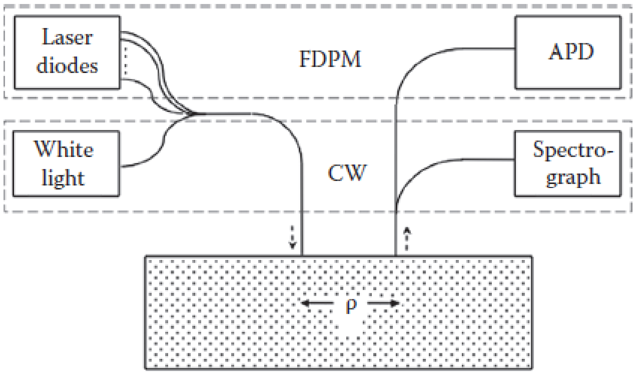

Figure 9: Diagram of a combined CW-NIRS and FDPM (broadband DOS) probe[24]. FDPM is performed using the laser diode and spectrometer while white light reflectance spectroscopy

Figure 9 is a block diagram describing how FDPM and CW-NIRS are integrated. FDPM is performed using the laser diode and avalanche photodiode (APD) while white light reflectance spectroscopy is performed using the lamp and spectrometer. FDPM provides absolute optical properties μ_a and μ_s' by use of a broad-bandwidth frequency sweep[4,5,15] (typically in the domain of 50-1000 MHz). The amplitude and phase as measured using a network analyzer or similar method is collected and compared against diffusion-based models. Representative data from this process is shown in figure 10a-b. Over several laser wavelengths (λ_{LD}), a power law can be fitted, resulting in reduced scattering across the near-infrared spectrum $\mu_s'(\lambda_{NIR})$. The effect of $\mu_s'(\lambda_{NIR})$ can be separated from attenuation, yielding a reflectance spectrum. The reflectance spectrum is then fitted to $\mu_a(\lambda_{LD})$, resulting in absorption across the near-infrared spectrum $\mu_a(\lambda_{NIR})$. Tissue composition is finally quantified using a four-component linear fit considering HbO2, HbR, H2O, and FAT. This process is depicted in figure 10c-d.

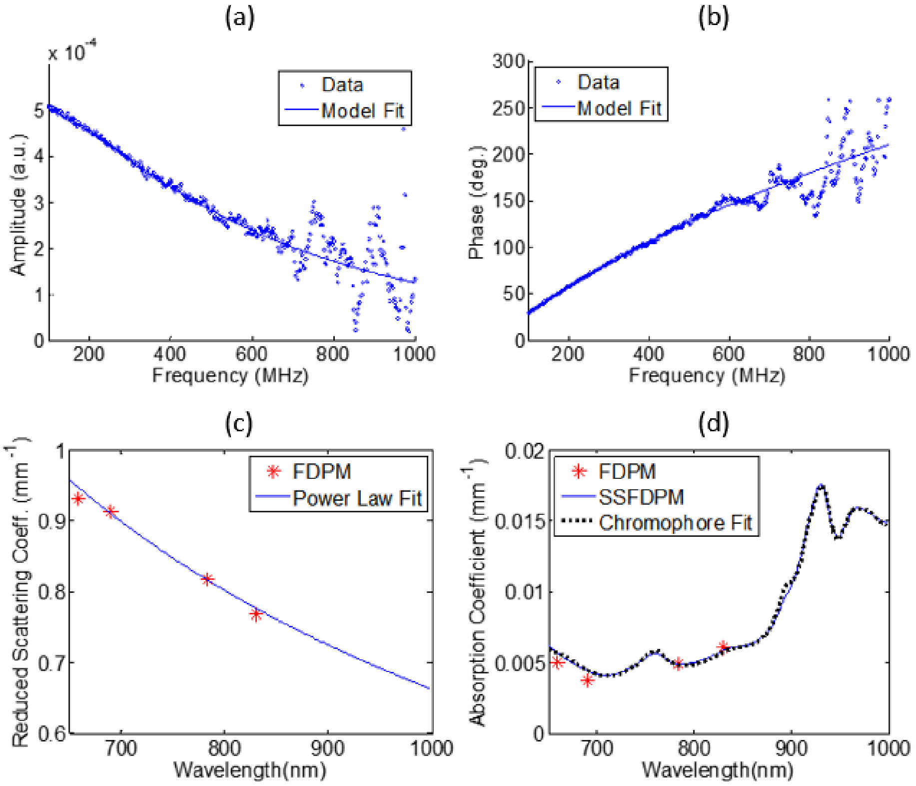

Figure 10: An overview of signals from a combined FDPM and CW-NIRS instrument measured on human abdomen[25] (a) Amplitude and (b) phase (blue dots) are fit using diffusion-based models (blue line) over a broad frequency range(c) A scattering power law (blue line) is fit to FDPM-provided μ_s' values (red asterisks) in order to determine tissue scattering across the NIR spectrum (d) The absorption spectrum is recovered by separating scattering from reflectance (blue line) and fitting the resultant to FDPM-provided μ_a values (red asterisks). Tissue composition is quantified using a four-component linear fit (dashed black line) considering HbO2, HbR, H2O, and FAT.

CHAPTER 2: Benchtop to bedside DOSI

Introduction

Frequency-domain photon migration (FDPM) is an established technique for performing quantitative noninvasive optical spectroscopy of tissue. By utilizing a model of photon propagation in multiple scattering media, FDPM can accurately estimate the absolute near-infrared absorption (μ_a) and reduced scattering (μ_s') properties of turbid tissue[14,26,27]. FDPM requires optical sources to be modulated at megahertz to gigahertz frequencies for accurate optical property assessment; therefore, discrete lasers are typically utilized as light sources. This imposes practical limitations on the spectral resolution of the technique and the total number of chromophores that can be measured simultaneously. By combining FDPM with broadband continuous-wave near-infrared spectroscopy (CW-NIRS), accurate optical property measurements over a wide near-infrared band (650-1000 nm) have been demonstrated[1].

In this work, we report a significant reduction in the size and weight of quantitative broadband NIRS by presenting a miniature diffuse optical spectroscopy and imaging (MDOSI) instrument that integrates FDPM at four discrete wavelengths with CW-NIRS from 650-1000 nm. The new system weighs 7.5 kg and is small enough to fit in a carry-on suitcase for air travel (14 x 33 x 43 cm) without sacrificing accuracy or precision of much larger systems. This greatly increases the portability of this powerful technique, lowers its barrier to access, and enables point-of-care clinical investigations. Based upon a custom multi-wavelength, multi-frequency (50-500 MHz) FDPM module[5], the MDOSI design has been replicated 16 times and it is utilized in preclinical and clinical investigations of military medicine[28,29], weight loss[30], sports medicine[31], and breast cancer[32–35]. In subsequent sections of this article we describe the design and fabrication of the MDOSI platform, report comprehensive performance metrics of accuracy and precision utilizing tissue-simulating phantoms, and show human subject measurements.

Materials and Methods

Hybrid FDPM and CW-NIRS

Bevilacqua et al[1] first described the combination of CW-NIRS with discrete wavelength FDPM to achieve quantitative broadband optical property estimation in living tissue. In FDPM, intensity modulated near-infrared laser light is injected into a turbid medium such as tissue. Multiple-scattering of the modulated source results in spreading spherical waves of photons called photon density waves (PDW)[26,36]. After interacting with the medium, diffusely reflected light is captured at a fixed distance away from the source, typically by a photodiode, avalanche photodiode (APD), or photomultiplier tube. The bulk optical properties of the medium are directly related to the measured amplitude attenuation and phase-shift of the PDWs by a radiative transport equation (RTE) for photons[23,36–38]. In this work, we utilized the P_1 approximation to the RTE in semi-infinite geometry[39], valid for multiple scattering tissue, to estimate μ_a and μ_s' at the FDPM laser wavelengths. A broadband (650-

1000nm) fit of the FDPM μ_s' to an inverse power dependence on wavelength ($\mu_s'(\lambda) = A \cdot \lambda^{-b}$) provides a good estimation of the broadband reduced scattering spectrum of the medium[10,11]. Subsequently a fiber-coupled broadband light source and spectrometer are utilized to collect broadband CW-NIRS diffuse reflectance at the same source-detector separation as FDPM. The CW-NIRS diffuse reflectance is corrected for scattering by using the FDPM-extracted reduced scattering spectrum and similar approximations to the RTE[12,40]. After correction, since the spectrometer does not provide an absolute measurement of optical power, the FDPM μ_a values provide the correct magnitude of the broadband absorption spectrum. Thus, the result is a quantitative measurement of $\mu_s'(\lambda)$ and $\mu_a(\lambda)$ continuously across the range of the spectrometer (currently 650-1000nm). In tissue, chromophores HBO2, HbR, H2O, and FAT are extracted from $\mu_a(\lambda)$ using linear least-squares optimization[1].

FDPM and CW-NIRS Calibration

FDPM subsystem is calibrated by use of tissue-simulating silicone phantoms with pre-determined optical properties[41,42]. The theoretical FDPM response of the phantom (i.e. amplitude and phase as a function of modulation frequency) is calculated using the P1 semi-infinite approximation. The deviations, which comprise the instrument response function (IRF), between the actual measurement and the ideal phantom response are used to correct all subsequent measurements in that session. This approach assumes that the IRF does not change between calibration measurements (typically at the beginning and end of a 1-2 hour session), or with change in detected signal level (i.e. attenuation of the medium). CW-NIRS calibration is achieved by use of a commercial reflectance standard measured prior to each measurement session.

MDOSI design and fabrication

The MDOSI system integrates all of the components necessary to perform the hybrid FDPM/CW-NIRS technique described in 2.2 (Fig. 11). Raw data (uncorrected multi-frequency FDPM amplitude and phase, CW-NIRS spectrometer counts) are passed to a personal computer (PC) where custom software orchestrates data acquisition and processing. The major components of the MDOSI system include a custom-built FDPM module[5], 1 mm circular diameter APD (C5658 with S6045-03 APD, Hamamatsu Photonics, Hamamatsu, Japan), tungsten-halogen broadband lamp (HL-2000-FHSA, Ocean Optics, Largo, FL), near-infrared spectrometer (HS2048XL-U2, Avantes, Apeldoorn, Netherlands).

The design of the multi-frequency FDPM module has been previously described[5]. Briefly, the FDPM module is capable of modulating (50-500 MHz) four internal semiconductor diode lasers (660, 690, 785, and 830 nm) with up to 15 dBm RF output. Average optical power for each laser is set for 20 mW at the fiber-coupled probe. Amplitude and phase are measured at a 50-ohm radio-frequency (RF) input utilizing an analog heterodyne demodulation approach to perform FDPM. An Arduino Due microprocessor (Arduino, Somerville, MA) coordinates the frequency sweep, digitizes the results, and manages data transfer to the PC over USB. Additional supporting electronics include a power supply (NV14G5TT, TDK-Lambda, Chuo-ku, Tokyo, Japan), thermal-electric controller (TCXX-PR-59, LairdTech, Chesterfield, MO) to stabilize the temperature of an external APD module, USB 2.0 hub (ST4200USBM, StarTech, Lockbourne, Ohio), and cooling fans. All components are housed in a custom chassis. Excluding the PC, the instrument measures 14 x 33 x 43cm and weighs 7.5 kg.

In this work, FDPM laser sources were coupled using an optical fiber bundle composed of 400 μm diameter, 0.37 NA fibers (LEONI Fiber Optics Inc., Williamsburg, VA). Broadband light was delivered using a 3 mm diameter fiber optic bundle composed of 50-micron fibers (0.55 NA) while a solid-core 1 mm (0.37 NA) optical fiber was used to guide CW reflectance light to the spectrometer. FDPM source and detector components are placed in cross-configuration relative to the CW-NIRS source and detector optical fibers to co-register measurement volumes. The probe allows the user to select source-detector separations of 22, 28, and 34 mm. 22 mm separation was used for phantom measurements and 28 mm for human breast tissue measurements.

CW-NIRS and FDPM are performed sequentially in order to prevent optical cross-talk between the two techniques. First, a CW-NIRS dark-corrected reflectance spectrum is acquired. If necessary additional spectra are automatically collected after adjusting the integration time to optimize spectrometer counts (e.g. 200 milliseconds). Then, the FDPM measurement proceeds in which each laser is sequentially modulated at 451 evenly spaced frequencies from 50-450 MHz to capture frequency and wavelength dependent amplitude and phase. An entire 4-wavelength FDPM measurement including software delays takes 1.2 s.

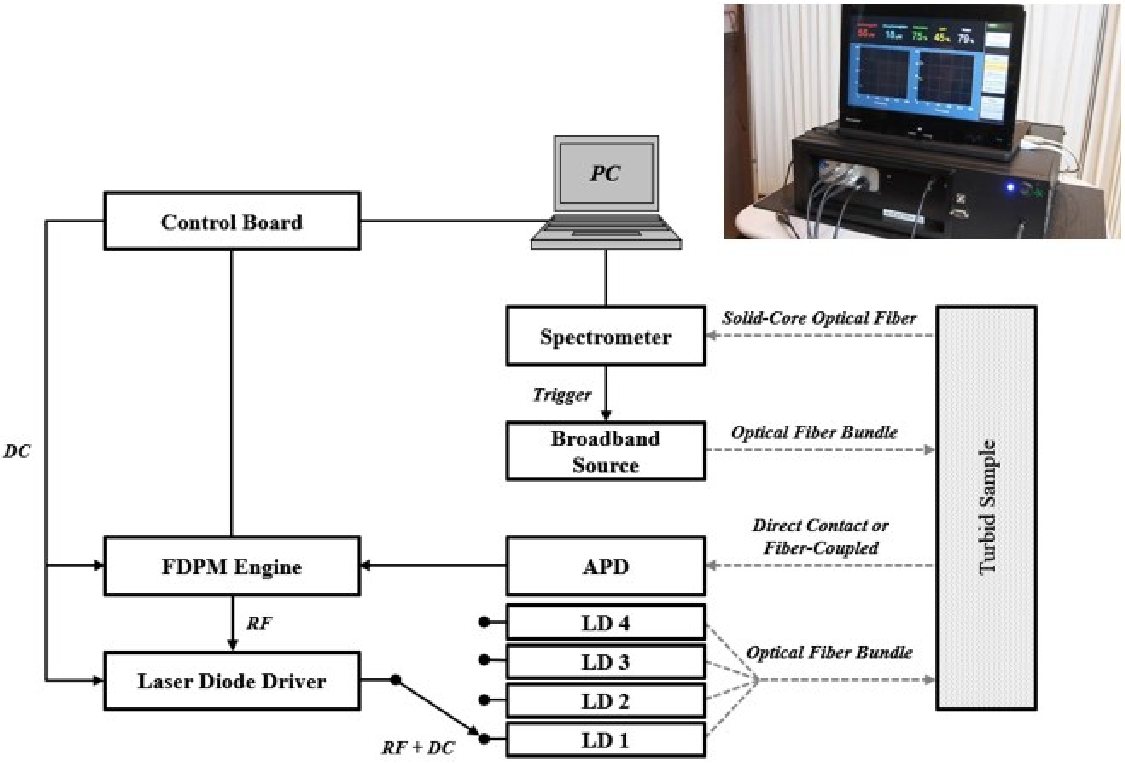

Figure 11: The system block diagram of the MDOSI system. Black lines denote electrical signals, grey dashed lines denote optical signals. A reference picture of the instrument is provided at the top-right.

Performance Assessment

The dynamic range (DR) of the MDOSI FDPM subsystem was assessed by progressively increasing attenuation between the source fiber and detector with two variable neutral density filters (NDC-50C-4, Thorlabs, Newton, NJ) at a fixed 50 MHz modulation frequency. Variations in the source power or filter attenuation was corrected using an optical power meter as a reference.

The MDOSI was validated against a "gold-standard" quantitative broadband DOS instrument. This system, which operates on the same hybrid FDPM/CW-NIRS principle, is based on an off-the-shelf radio-frequency vector network analyzer and has been validated previously[1,43]. For comparison, this system weighs over 100 kg and is housed in a server rack approximately 48 x 30 x 25 inches. For consistency, the same direct-contact probe containing the 1 mm diameter APD was utilized for both systems. Both systems were calibrated by use of the same silicone tissue-simulating phantom and Spectralon-based reflectance standard (AS-01161-060, Labsphere, North Sutton, NH). Accuracy was determined by measuring three optically-varied silicone-based tissue-simulating phantoms with both MDOSI and the gold-standard system.

Stability/precision was assessed by measuring a single phantom continuously over the course of one hour at a fixed probe position. For the FDPM subsystem, amplitude and phase precision was represented as percent change with respect to the first measurement. All stability tests were performed after a 30 min warmup delay. For CW-NIRS subsystem, as the integration time of the spectrometer is dynamically adjusted throughout a continuous measurement, precision was evaluated by calculating the percent difference of the raw spectrometer counts with respect to the first measurement.

Long-term repeatability of an MDOSI instrument was assessed by collecting 41 measurements over 11 months (approximately weekly) on three tissue-simulating phantoms by a single experienced operator. Each phantom was measured three times per session, with the probe placed and replaced each time, in order to account for variability in probe position and pressure.

Normal human breast tissue of a premenopausal subject was measured using both the MDOSI and gold-standard sequentially on the same day. Data acquisition methodology (e.g. breast gridding) was identical to the breast imaging approach employed in ACRIN-6691 multi-center study utilizing DOSI technology[33]. Measurements on breast tissue were taken on a 10 mm spaced square grid in an 80 x 60 mm area (48 total pixels).

Results:

FDPM Subsystem Dynamic Range (DR)

We first assessed the DR of the MDOSI system to determine the range of tissue attenuation (i.e. tissue types) and source-detector separations that can be measured. Overall DR is limited by the FDPM subsystem since spectrometer has a dynamically adjustable integration time to maximize SNR. FDPM DR was measured for all 4 wavelengths at a fixed 50 MHz modulation frequency (Fig. 12). DR is expressed in decibels (dB) calculated by $dB = 20 \times log\left(\frac{A}{A_{nf}}\right)$ where the noise floor amplitude (A_{nf}) was calculated for the APD by an average of 10 noise measurements to mitigate effects of random amplitude fluctuations of the noise floor. For all wavelengths, DR was approximately 70 dB, and LDR was approximately 60 dB.

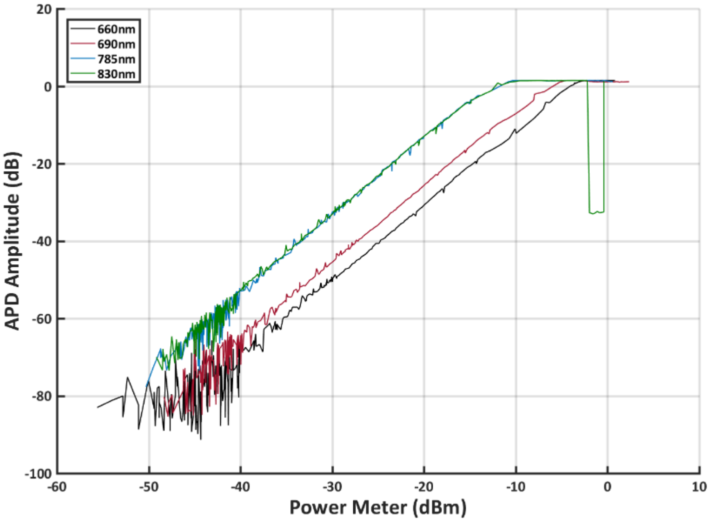

Figure 12: Dynamic range of the MDOSI APD measured using the 4 laser diodes housed in the MDOSI at 50 MHz modulation frequency compared against a power meter reported as dBm.

System Accuracy Performance

Optical properties three tissue-simulating phantoms (labeled A, B, and C) were obtained using the gold standard instrument (Fig. 13a-b). μ_a and μ_s' spectral differences between the MDOSI and reference instrument (i.e. $\Delta\mu_a = \mu_{a\ MDOSI} - \mu_{a\ Ref}$) are shown (Fig. 13c-d). For μ_a, accuracy was within 0.0003±0.0001, 0.0008±0.0002, and 0.0008±0.0002 mm^{-1} for phantoms A, B, and C, respectively with the highest error occurring at the 908 nm silicone absorption peak. Accuracy for μ_s' was 0.008±0.001, 0.007±0.004, and 0.006±0.003 mm^{-1} for phantoms A, B, and C, respectively.

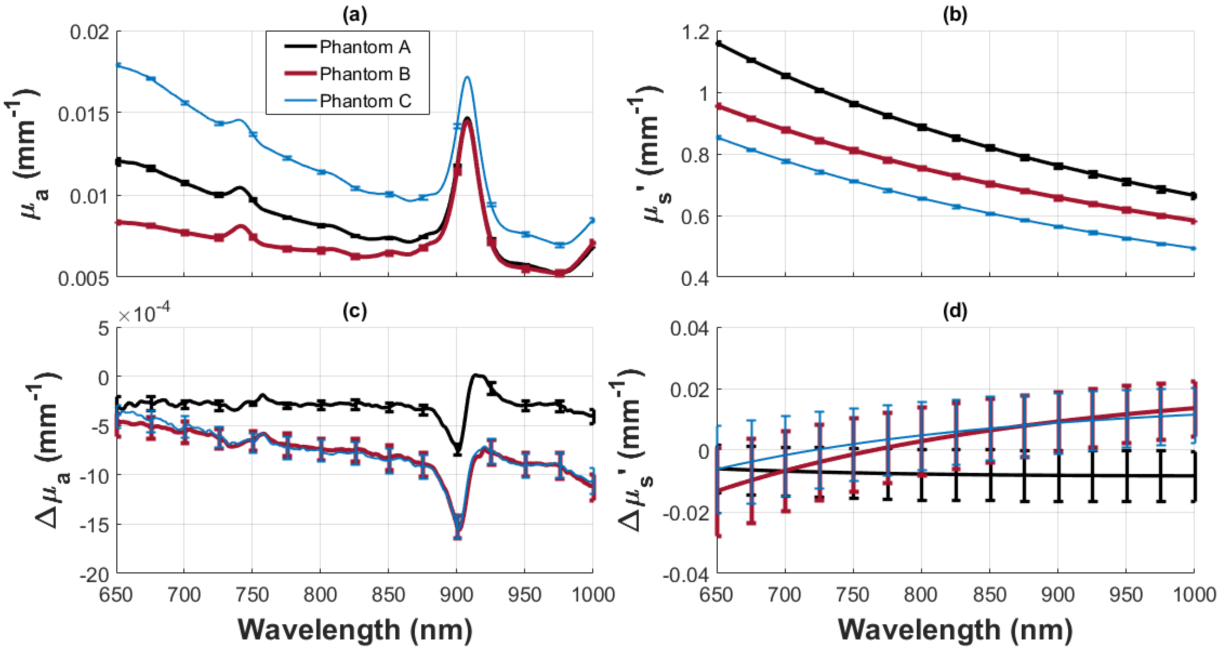

Figure 13: Three phantoms were utilized to gauge the accuracy of the MDOSI with respect to the gold-standard instrument. The phantoms were measured three times by both instruments using an identical probe set at a 22 mm SDS. (a,b) The optical properties of three silicone-based tissue simulating-phantoms measured by the standard system. (c,d) Differences in optical properties of three tissue-simulating phantoms between the MDOSI and gold-standard device.

System Stability and Precision

To determine system stability, an optical phantom was continuously measured by the MDOSI device over the course of 1 hour at a rate of 1 measurement every 30 seconds. The greatest standard deviation (n=120) for a continuous measurement on a single phantom over the broadband range was observed to be 0.0001 mm^{-1} and 0.0058 mm^{-1} for μ_a and μ_s', respectively, and occurred at 650 nm where attenuation was greatest (Fig. 14a-b). FDPM subsystem precision was also investigated. FDPM amplitude precision, calculated at 50 MHz modulation, ranged from 0.26±0.20% to 1.44±0.59%, depending on wavelength. Similarly, phase precision ranged from

0.13±0.10% to 0.28±0.16%. Spectrometer precision ranged from <0.01% to 4.49±2.32%. For weekly measurements over the course of 11 months, the maximum standard deviation occurred in the highest attenuating phantom, with 0.0007 mm^{-1} and 0.0174 mm^{-1} for μ_a and μ_s', respectively (Fig. 4c-d).

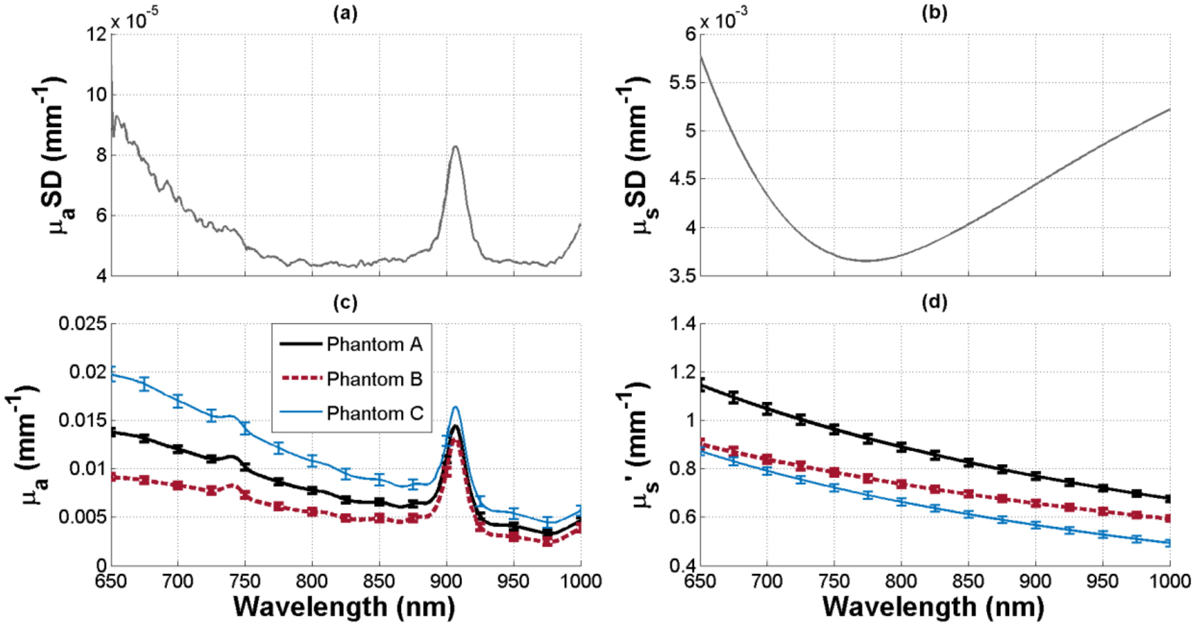

Figure 14: (a-b) μa and μs′ standard deviation of 120 broadband measurements by the MDOSI device taken over the course of 1 hour. (c-d) Broadband optical properties of three phantoms measured by a single operator and single MDOSI instrument from 41 sessions over the course of 11 months. Error bars are reported as standard deviation.

In vivo validation

Healthy breast tissue was imaged using the MDOSI and gold-standard device. Both devices followed a 6 x 8 cm grid pattern with measurement points spaced every 1 cm. Extracted chromophore concentrations as well as a histogram of chromophore differences by pixel between the two instruments are shown (Fig 15). Overall, the average difference between instruments (MDOSI minus gold-standard) was 6.7±2.0 μM, 0.4±0.8 μM, 2.0±4.1, and -2.4±6.5 for HBO2, HbR, H2O, and FAT, respectively.

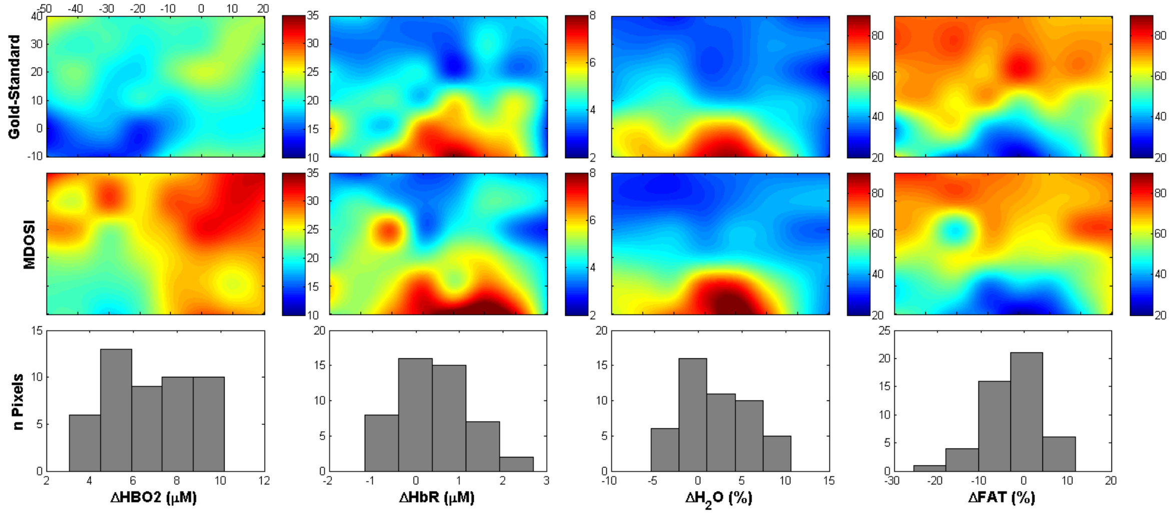

Figure 15: Interpolated DOSI images of normal breast tissue composition in a premenopausal subject captured with the gold-standard (top row), MDOSI (middle row), and a histograms of the pixel-to-pixel chromophore differences (bottom row). Physical coordinates of the measurements are shown in millimeters in the top left graph.

Discussion

In this work, we describe the design and validation of a portable device for quantitative broadband diffuse optical tomography of human tissue. The MDOSI instrument integrates all of the components necessary to complete hybrid FDPM / CW-NIRS and capture the optical absorption and reduced scattering spectra of tissue continuously from 650 to 1000 nm utilizing a handheld optical probe. We were motivated to developed this device to: 1) reduce cost and complexity barriers of quantitative tissue optical spectroscopy, 2) significantly increase portability, and 3) facilitate the advancement of Biophotonics research in clinical applications worldwide[43].

The MDOSI was designed to be run by users with minimal Biophotonics background, which remains an important factor for increasing the adoption of tissue spectroscopy in clinics and multidisciplinary labs. MDOSI measurements are triggered and displayed through a custom graphical user interface installed on a Windows PC. The included software was designed to guide users through the necessary calibration steps, provide semi-automated naming schemes to organize files, automatically adjust integration time for the spectrometer, and warn the user if the data is detected to be abnormal in quality. Two different measurement schemes can be configured, which includes time acquisition for a single-point dynamic measurement, or a grid-imager which is used for wide-area imaging studies.

In order to capture a wide variety of tissues types without necessitating gain adjustments (and likely recalibration) to the optical detector or light source, a large DR is preferred. DR for the 660nm was shifted towards higher optical powers due to the slightly lessened quantum efficiency of the APD at 660nm compared to other wavelengths in the system. LDR for all wavelengths was still approximately 60 dB. This DR is suitable for measuring a variety of adipose tissue types ranging from approximately 10-30 mm on adipose tissue and 10-20 on highly vascularized tissue. For example, within a single measurement session, at least 30 dB of dynamic range is necessary for capturing hemodynamic changes resulting from the common arterial/venous occlusion challenge to assess oxygen metabolism.

Optical property accuracy was assessed by measuring a common set of tissue-simulating phantoms and in vivo human breast tissue with the MDOSI and an independently-validated system. Phantoms were selected to cover a range of typical tissue optical properties, including breast and muscle tissue. On average, across the NIR spectrum, the two instruments agreed well within 10% of optical properties. Some sources of error include amplitude and phase drift as previously detailed[5] as well as more wavelengths for the previous generation system, which may prove advantageous for reduced scattering and absorption spectrum fitting. This accuracy is comparable to that of other large format quantitative broadband DOS systems. For example, broadband time-domain[44] has been reported to accurately recover tissue optical properties with 7 to 10% accuracy.

Short (~1 hr) and long (~1 yr) term stability performance of a single MDOSI instrument was evaluated by repeatedly measuring a set of silicone tissue-simulating phantoms. Short-term stability was excellent, deviating less than 0.0001 mm^{-1} and 0.0058 mm^{-1} for μ_a and μ_s', respectively, variation in optical properties equating to <2% system drift. The greatest discrepancies were observed near the 908 nm silicone absorption feature, which may be attributed to the increased attenuation and decreased SNR at this wavelength. Although “short-term” was defined as one hour, typical system stability was discovered to be relatively independent of time once the system reached equilibrium temperature. Thus, system drift is expected to remain at or below

2% beyond one hour of continuous measurement. FDPM amplitude and phase precision was found to be excellent, with amplitude precision within 2%, and phase precision within 0.3%. Our results are comparable to a report by Leproux et al. in which a large-format DOS device drift measurement on a single phantom calculated system precision for μ_a and μ_s' to be within 0.0010 mm^{-1} and 0.01 mm^{-1}, respectively[43]. Precision of CW-NIRS in the MDOSI relies primarily on spectrometer performance. The integration time of the spectrometer is dynamically adjusted from measurement to measurement in an attempt to maintain a high signal-to-noise ratio (SNR). While absolute "counts" level cannot be compared between measurements, the recovered near-infrared spectrum should remain steady on a static phantom regardless of integration time. In other words, CW-NIRS precision was determined using the consistency of the acquired CW-NIRS spectrum as the metric. CW-NIRS precision was <0.5% averaging across all wavelengths. Variability was observed to be greatest on attenuated wavelengths near hemoglobin absorption peaks (<700nm) whereas highest precision was achieved when SNR was greatest in the 800-850nm region.

For a much longer-term evaluation of the MDOSI device stability, 41 separate measurements were performed over 11 months on a set of optically varied phantoms. The highest optical property deviation resulted from the phantom with the highest absorption signature. Other sources of variation include possible inconsistent instrument setup for each measurement session (such as loose optical or electrical cables), operator errors such as minor shifts in the measurement location on the phantoms, and contact variations. Overall, the MDOSI demonstrated a high degree of stability over an 11-month period.

An interpolated image of 80 x 60 mm premenopausal breast data is shown (Fig. 15). It should be noted that a single abnormal pixel was detected, seen at coordinates (-30, 20) in the gold-standard data, which may have been due measurement errors such as probe placement or poor contact between the probe and the tissue. Although the same subject was measured using both instruments within the same hour, an unavoidable source of discrepancy between the two instruments may be attributed to spatial and temporal biological variation. Another potential factor may be various degrees of probe contact. Analyzing the images from both instruments, the areola was particularly pronounced in the H2O and lipid maps at (-10, -10). Overall, the MDOSI and previous generation instrument produced similar chromophore maps on the same subject, with high contrast regions captured by both instruments corresponding to real anatomical structures.

Limitations of the study include use of a single MDOSI instrument in comparison to the gold-standard device. In addition, the gold-standard device utilizes the same type of frequency-domain optical techniques as housed in the MDOSI. Both instruments could potentially be subjected to the same biases, thus a more robust approach would involve additional optical methods such as time-domain or multi-distance. However, Leproux et al.[43] and Cerussi et al.[41] have extensively investigated DOS devices duplicated by our group concluded equivalence between instruments.

Conclusion

The MDOSI represents a clinical-friendly device built for translational science, relocating cutting-edge Biophotonics from the benchtop to clinics worldwide. Significant effort has been invested in improving usability by establishing standardized calibration and data acquisition procedures[41]. This has resulted in the adoption of the MDOSI platform in research sites internationally[32,43]. Miniaturization of the device have resulted in a reduction of the instrument footprint to a form-factor suitable for transportation by hand with similar precision and accuracy when compared to the previous generation. Further work on ease-of-use has allowed for the international adoption of the MDOSI, providing advanced tissue spectroscopic tools for researchers and clinicians.

CHAPTER 3: High-speed, multi-modal DOSI

Multi-modal diffuse optical spectroscopy for high-speed monitoring and wide-area mapping of tissue optical properties and hemodynamics (*in submission*)

Jesse H. Lam[a], Brian Hill[b], Robert Amelard[c], Sehwan Kim[a,d], Seonguk Cho[d], Timothy Quang[b], Hossein S. Yazdi[a], Robert V. Warren[a], Kyle B. Cutler[a], and Bruce J. Tromberg[a,b,*]

[a]University of California, Irvine, Beckman Laser Institute, Department of Biomedical Engineering, Irvine, CA, USA

[b]National Institutes of Health, National Institute of Biomedical Imaging and Bioengineering, Bethesda, MD, USA

[c]Western University, Department of Biophysics, London, Ontario, Canada

[d]Dankook University, School of Medicine, Cheonan-si, Chungnam, Republic of Korea

Abstract:

Lack of instrument flexibility is a key limitation of DOSI for clinical and pre-clinical studies. Current broadband diffuse optical spectroscopic imaging (DOSI) devices do not provide sufficient acquisition rates to capture pulsatile biomedical signals. In addition, generating chromophore maps is a laborious process requiring 20-40 minutes to capture 100-200 points over a 10 cm square area. We designed a high-speed DOSI instrument that can capture broadband spectra, high-resolution imaging, and dual-channel hemodynamics. Following system designs, we then characterize the system performance with heterogeneous optical phantoms and *in-vivo* models. High-resolution optical property maps of absorption (μ_a) and reduced scattering (μ'_s) was recovered on phantoms with embedded objects by capturing over 1000 measurement points in under 5 minutes. To demonstrate multi-layer sensitivity, we imaged human calf tissue with a 4.8 mm skin-adipose thickness, showing the two layers have significantly different ($p<0.001$) total hemoglobin and μ'_s composition. Finally, human thenar tissue was measured using a combined broadband DOSI and continuous-wave near-infrared spectroscopy method (~15 Hz acquisition rate) to calculate tissue arterial oxygen saturation, venous oxygen saturation, and tissue metabolic rate of oxygen consumption during baseline and after release of an arterial occlusion. We conclude that a DOSI device which allows for accessible and efficient acquisition of multi-modal datasets provides a more complete picture both spatially and temporally of heterogeneous and layered tissue.

Keywords: Diffuse optical spectroscopy, imaging, chromophore, near-infrared, multi-modal, hemodynamic, oximetry, tissue metabolism

1. Introduction

Diffuse optical spectroscopic imaging (DOSI) is a versatile technology that non-invasively monitors tissue hemodynamics and has a wide variety of clinical applications. One type of application involves wide-area (centimeter scale) chromophore mapping of tissue. For breast cancer studies, DOSI can monitor the effects of neoadjuvant chemotherapy[32,33,45,46]. In addition, characterization of tissue layers, such as breast adipose and the underlying tumor, can also provide unique insights. For example, in previous work using a DOSI-guided differential diagnosis method, the broadband spectral differences between a breast with a benign or malignant tumor and the contralateral normal breast were analyzed[6]. The conclusion was that DOSI may offer data to supplement standard-of-care methods to determine whether a tumor is benign or malignant. However, breast tissue in that study was considered homogenous, and only bulk optical properties were assessed. We hypothesize that further studies of similar nature may see greater differentiation power (benign or malignant) given the ability to separate the pure spectra of embedded tumors from surrounding adipose tissue. In addition, other groups have expressed interest in separating tissue layers using multiple source-detector separations (SDS)[47–51]. Without the capability to capture at multiple SDS, differentiation of centimeter deep stratified structures is difficult without complex methods such as time-of-flight analysis in picosecond time-domain systems and gigahertz-capable network analyzers in the frequency-domain[52,53].

Another type of application involves a time-series, fixed-position DOSI probe to monitor tissue dynamics over time. For example, optically obtained hemodynamic biomarkers have been identified as key indicators of hemorrhage and resuscitation[28,29,54–56]. However, for continuous time measurements at a single point, clinical DOSI instruments[1,5] fall well below the temporal resolution required to resolve pulsatile hemodynamics[57,58]. Without pulsatile hemodynamics, arterial oxygenation (*SaO2*) and venous oxygenation (*SvO2*) – two fundamental physiological parameters related to oxygen supply and delivery[59,60], respectively – cannot be readily assessed optically. Without *SaO2* and *SvO2*, the oxygen extraction fraction (*OEF*) cannot be easily determined[61,62]. The *OEF* is also needed to calculate the tissue metabolic rate of oxygen consumption (*tMRO2*), a direct measure of tissue metabolism by accounting for the OEF and local blood flow[61,63].

Instrument constraints, such as data acquisition speed, limit the scope of DOSI applications for clinical and pre-clinical studies. Synthesizing chromophore maps must be done manually in a point-by-point fashion which is both time and resource intensive. Mapping tissue at multiple SDS further extends the measurement time. In addition, without supplementary instruments to gauge the magnitude of blood flow, such as diffuse correlation spectroscopy (DCS)[64,65], it is challenging to estimate *tMRO2* with traditional DOSI devices.

To expand the scope of DOSI in applications such as including pulsatile hemodynamics in hemorrhage studies[28,56], or supplementing broadband breast cancer imaging with layer separation ability[33,66], advancements in DOSI instrumentation are needed to develop a multi-modal, flexible spectroscopic imaging device capable of multiple SDS views. Here, we develop and validate a high-speed DOSI instrument capable of broadband spectroscopy, higher resolution chromophore and optical property imaging, rapid-hemodynamic, *SaO2*, *SvO2*, and *tMRO2* analysis. These modes can be selectively switched allowing for multiple modalities at varying spatial and temporal scales to be rapidly captured on patients in one session.

2. Materials and Methods

2.1 *DOSI Instrumentation*

DOSI is a well-established quantitative optical technique which utilizes frequency-domain photon migration (FDPM) and continuous wave (CW) methods to recover absorption (μ_a) and reduced scattering coefficients (μ'_s) across the near-infrared spectrum (600 – 1000 nm). The theory and implementation of DOSI has been extensively reported in previous literature[15,26,67]. Briefly, FDPM utilizes discrete near-infrared light sources such as laser diodes in the MHz to GHz regime. By comparison of the amplitude decay and phase shift to a reference as a function of frequency, the P1 semi-infinite approximation to the radiative transport equation can be fit to the data and recover optical properties[12,26]. Given a sufficient number of wavelengths, concentrations of tissue chromophores such as oxyhemoglobin (*HbO2*), deoxyhemoglobin (*HbR*), water (*H2O*), and lipid (*FAT*) present in turbid media can be separated and quantified by least-squares fitting using known extinction coefficients[15].

The DOSI instrument houses two laser diode channels with six total lasers – a pair of 3 laser diodes with wavelengths centered at: 727 nm, 808 nm, and 839 nm. Laser light was guided by use of custom 8-to-1 optical fiber bundles comprised of 400 µm optical fibers (R Specialty Optical Fibers LLC, Williamsburg, VA). Laser operation was regulated by a commercial laser diode controller (LDC-3916, Newport Corporation, Irvine, CA). Radio frequency (RF) modulation (50-500 MHz) provided sequentially to each laser diode at 3 dBm was achieved by use of a network analyzer (TR1300/1, Copper Mountain Technologies, Indianapolis, Indiana). Modulated laser light was collected using a 1 mm solid-core fiber optic cable coupled to an avalanche photodiode (APD) (S11519-30 APD with custom module, Hamamatsu Photonics K. K., Hamamatsu City, Japan). In broadband spectroscopic mode, output from a tungsten-halogen lamp (HL-2000-FHSA, Ocean Optics Inc., Largo, FL) with resulting diffuse reflectance was routed using a 1 mm solid-core fiber optic cable to a commercial spectrometer (HS2048XL-U2, Avantes, Apeldoorn, Netherlands). A consumer laptop computer (Razer Blade Pro 17, Razer Inc., San Francisco, CA) was used to operate the instrument and acquire data.

2.2. *DOSI Acquisition Parameters*

The network analyzer utilized provides RF modulation to each laser diode in the system sequentially at a speed of approximately 150-200 μs/point. Taking careful consideration to avoid aliasing of the FDPM phase component, we empirically determined (data not shown) that 200 evenly distributed sampling points spanning 50-500 MHz optimized network analyzer acquisition speed. Other significant instrument delays in the system were due to the slow-start logic in the laser diode controller. In order to stabilize the laser diode and prevent undesirable electrical spikes, the laser diode current is increased incrementally over several hundred milliseconds until the user-defined current is reached. To bypass this, the average optical power level of the lasers was maintained at 30 mW throughout measurements, thus the acquisition speed of the system was ultimately limited by the maximum frequency sweeping time of the network analyzer.

The integration time of the spectrometer can range from hundreds of milliseconds on low attenuating tissues such as adipose, to thousands of milliseconds on highly attenuating tissues such as muscle. In many instances, integration time of the spectrometer is the most significant factor which limits DOSI acquisition speed. To mitigate this, a CW near-infrared spectroscopy (CW-NIRS) laser method was adopted in conjunction with broadband DOSI for rapid-acquisition measurements. Due to the modulation rate of the laser light in the MHz regime, the effects of modulation were not perceivable by a spectrometer operating at tens of Hz; thus, modulated laser light from the point of view from the spectrometer can effectively be considered CW. In this mode, acquisition rate can be up to 15 Hz, depending on how often quantitative measurements (broadband DOSI or FDPM) are taken. Tissue chromophores were extracted from the DOSI measurement using linear, least-squares fitting[15] and the differential path length factor method when handling the CW-NIRS data[68].

2.3. *Optical Phantom Fabrication*

Two silicone-based solid optical phantoms with suspended equilateral cross-shaped silicone inclusions were fabricated for DOSI imaging experiments. Our tissue-simulating silicone phantom construction process has been described previously[41]. We used Nigrosin (Sigma-Aldrich, St. Louis, MO) and titanium dioxide (TiO_2, 44 microns, Loudwolf, Dublin, CA) for the absorbing and scattering agents, respectively. Figure 16a displays the dimensions for the cross-shaped inclusion. In addition, another 450 mL mold was filled using solution from the same batch to be used as a reference for optical characterization. The silicone was cured for a minimum of 24 hours. To fabricate the final phantom with the suspended inclusion, the cured cross-shaped silicone was submerged and held using pins at the desired depth within the background solution while it solidified. After 24 hours, the pins were removed. Two phantoms were fabricated, one with the inclusion suspended at a depth of 6 mm and another at 24 mm. Optical properties of the pure phantom background ($\mu_a=0.007\ mm^{-1}$, $\mu'_s=0.62\ mm^{-1}$) and pure inclusion ($\mu_a=0.033\ mm^{-1}$, $\mu'_s=0.32\ mm^{-1}$) were characterized using DOSI at 808 nm, giving an approximate inclusion-to-background contrast ratio of 4.7 and 0.5 for absorption and scattering, respectively.

2.4. *Optical Phantom Imaging Setup*

Figure 16b shows a 12 x 12 cm boundary drawn on the surface of the phantom. During image acquisition, the probe was maintained within the defined boundaries. A pair of 2 mm perforations were visible on the phantom surface due to the removal of the pins that suspended the inclusion during the curing process. An HTC Vive (Xindian District, New Taipei City, TW) tracked the motion of the probe during image acquisition. The setup consists of a "Lighthouse" infrared laser emitter and a detection unit. The HTC Vive utilizes a time-of-flight approach and distributed photodiodes around the detection unit to calculate position and orientation[69]. The Lighthouse was positioned 1 meter above the measurement plane while the detection unit was affixed to the probe (Figure 16c).

Data was captured at ~250 ms/pixel with the probe manually raster scanned throughout the acquisition area. The phantoms were measured at three different SDS: 8 mm (ρ_8), 16 mm (ρ_{16}), and 24 mm (ρ_{24}). For the phantom with the 6 mm deep inclusion, an additional scan was performed with an orthogonal source-detector orientation. The purpose of capturing this dataset is three-fold: 1) to illustrate differences in image resolution using a 1-cm grid method versus the proposed continually scanning method 2) to show sensitivity to different layers on a heterogeneous optical phantom and 3) to test whether having supplementary data from an orthogonal scan will improve image quality.

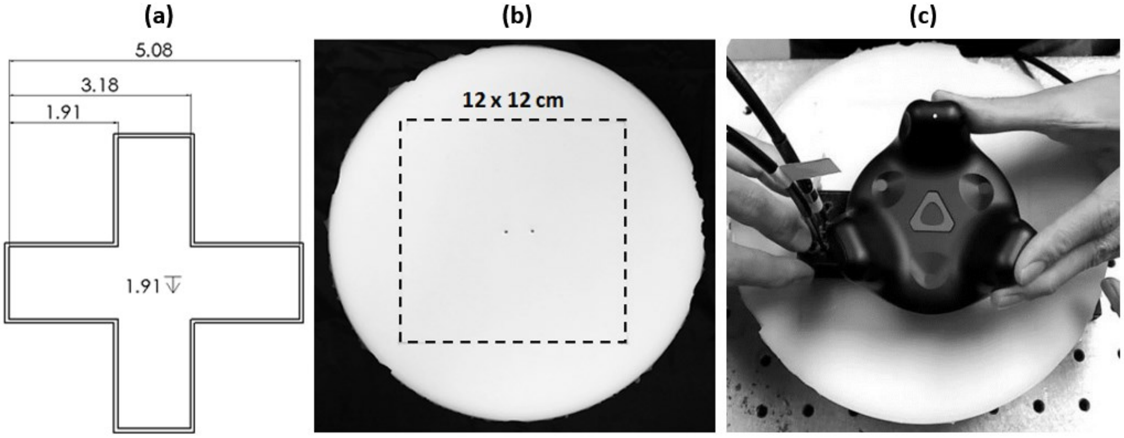

Figure 16: A silicone phantom with a cross-shaped embedded inclusion was fabricated. (a) The dimensions of the equilateral cross-shaped inclusion mold are defined in centimeters. (b) A 12 x 12 cm perimeter for the scanning area was drawn in which the DOSI probe was maintained within the boundaries during the raster scan. (c) The probe with attached source optical fiber, detection optical fiber, and HTC Vive detection unit. The HTC Vive Lighthouse was placed approximately 1 meter above the scanning surface (Lighthouse not captured in image frame).

2.5. *in vivo Imaging*

To illustrate dual-layer, heterogeneous imaging on calf, a 5 x 8 cm area on the medial gastrocnemius (calf) of a healthy human male subject was imaged with one DOSI channel at an SDS of 10 mm (ρ_{10}). The same region was then imaged again using an SDS of 20 mm (ρ_{20}). The subject was instructed to sit comfortably in a chair and rest his leg extended on a table while being imaged with the probe held similarly as shown in figure 1c. We measured skin and adipose tissue thickness with ultrasound (SonoSite Titan, Fujifilm SonoSite, Bothell, WA).

2.6. *in vivo Dual Layer Measurements*

Differences in hemodynamic response of two tissue layers (adipose versus mixed adipose and muscle) were demonstrated using an arterial occlusion measured by a dual-channel probe affixed to the center of the same calf area. The probe was configured to measure at ρ_{10} and ρ_{20}. After 90 seconds of baseline, a rapid occlusion cuff (AG101 pump with E20 regulator, Hokanson Vascular, Bellevue, WA) was inflated for 90 seconds, and then released for 90 seconds. The peak occlusion cuff pressure was set to 200 mmHg. In order to more accurately quantify hemoglobin, tissue water and lipid obtained using broadband DOSI was considered when fitting for absolute hemoglobin values[1]. A 3 x 2 cm grid with 1 cm spacing was also captured with broadband DOSI at the same SDS configurations.

2.7. *in vivo Rapid Hemodynamics*

Rapid hemodynamics were captured in order to assess tissue *SaO2*, *SvO2*, and *tMRO2* on a one-layer, homogenous model. This was achieved by a point measurement on the thenar during an arterial occlusion of the same subject monitored using a combined broadband DOSI and CW-NIRS approach at ρ_{24}, where broadband DOSI provided absolute quantification of tissue chromophores. The measurement timeline was as follows: a 60 second baseline, 90 second occlusion at 200 mmHg, and a 90 second recovery. *tMRO2* was calculated at baseline, occlusion, and recovery using only DOSI parameters, but also compared against *tMRO2* utilizing *rBF* measured by DCS. *tMRO2* calculations were derived from methods described previously[70]. An additional thenar occlusion was performed and blood flow was measured using DCS at ρ_{24}. The DCS instrument utilized a 785-nm long coherence length laser (Crystalaser, Nevada) with the optical output set to 30 mW. For detection, 4 single photon counting modules were connected to a 4-to-1 single-mode fiber bundle (SPCM-AQRH-15-FC, Excelitas, Canada). The digital outputs of the detectors were connected to a PCIe6612 (National Instruments, Austin, TX) and captured using a custom LabVIEW interface (National Instruments, Austin, TX) with an acquisition rate of 20 Hz. Given the expression:

$$tMRO2 = [O_2]_a \cdot \alpha \cdot rBF \cdot OEF \ (1)$$

Where $[O_2]_a$ is the molar oxygen concentration in arterial blood, α is a calibration factor relating relative to absolute blood flow, *rBF* is the relative blood flow, and *OEF* is defined as:

$$OEF = \frac{[O_2]_a - [O_2]_v}{[O_2]_a} \ (2)$$

$$[O_2]_a = 4 \cdot [tHb]_a \cdot SaO2$$

$$[O_2]_v = 4 \cdot [tHb]_v \cdot SvO2$$

$[O_2]_v$ is the molar oxygen concentration in venous blood, $[tHb]_a$ and $[tHb]_v$ is the total hemoglobin concentration in the arterial and venous system, respectively. *SaO2* and *SvO2* are the arterial and venous oxygen saturation fractions, respectively. Substituting equation (2) into (1), the expression for *tMRO2* simplifies to:

$$tMRO2 = 4 \cdot (SaO2 - SvO2) \cdot \alpha \cdot rBF \cdot [tHb]_a \; (3)$$

The parameter α can be determined by tracking the rate of *HbR* accumulation ($\frac{d[HbR]}{dt}$) during a zero-flow condition such as an arterial occlusion. Using the relationship between *tMRO2* and *HbR* ($tMRO_2 = 4 \cdot \frac{d[HbR]}{dt}$) for the first minute of an arterial occlusion[70], α can be solved and substituted into (3) to obtain:

$$tMRO2 = 4 \cdot (SaO2 - SvO2) \cdot \frac{\frac{d[HbR]}{dt}}{(SaO2-SvO2)_{bl} \cdot rBF_{bl}} \cdot rBF \; (4)$$

$(SaO2 - SvO2)_{bl}$ is the average difference between *SaO2* and *SvO2* during baseline, and rBF_{bl} is the average relative blood flow during baseline.

SaO2 can be optically obtained using DOSI by isolating the pulsatile hemoglobin signal and calculating the oxygen saturation ($SaO2 = \frac{HbO2a}{tHb_a}$) fraction in the human heartrate frequency band where $HbO2_a$ is the fraction of *HbO2* in the arteries[58]. SvO_2 was estimated by $tHb_a = (1 - \beta) \cdot tHb$ where β is arterial blood volume fraction, and *tHb* is the total hemoglobin (*HbO2*+*HbR*) as measured using DOSI. SvO_2 was calculated with β=0.3 from literature[51,71]. Furthermore, $HbO2_a$ can be calculated by $HbO2_a = tHb_a \cdot SaO2$.

Finally, SvO_2 can be calculated by removing the contribution of arterial oxygen saturation from the overall tissue saturation:

$$SvO2 = \frac{HbO2 - HbO2_a}{tHb - tHb_a} \quad (5)$$

rBF is a non-quantitative measure of relative blood flow and was estimated by DOSI:

$$rBF \propto tHb_{Pulse} = HbO2_{Pulse} + HbR_{Pulse} \quad (6)$$

tHb_{Pulse}, $HbO2_{Pulse}$, and HbR_{Pulse}, respectively, are the tHb, $HbO2$, and HbR introduced per heart pulse.

3. Results

3.1 Instrument Performance

In overview of the DOSI measurement modes, the instrument can acquire at ~0.5 Hz when using 3 laser diodes in full broadband spectroscopic mode, 4 Hz when using 3 laser diodes in continuous scanning mode, 2 Hz when using 6 laser diodes in dual-channel measurement mode, or 15 Hz when utilizing 3 diodes in combined broadband DOSI and CW-NIRS rapid hemodynamic mode, as summarized in table 1. Note that the method of broadband DOSI is unchanged from previous iterations of the DOSI device, with the capture rate dependent on the integration time of the spectrometer.

Mode	FDPM Lasers	CW Source	Capture Rate
Broadband DOSI	**727, 808, 839 nm**	**Lamp**	**~0.5 Hz**
Dual-Channel	**2 x (727, 808, 839 nm)**	**None**	**2 Hz**
Continuous Scanning	**727, 808, 839 nm**	**None**	**4 Hz**
Rapid Hemodynamics	**727, 808, 839 nm**	**FDPM Lasers**	**15 Hz**

Table 1: DOSI modalities and capture speed utilizing various light sources available in the system. The modes can be selected on-the-fly to facilitate multi-modality data collection in a single measurement session.

3.1. *Phantom Imaging Results*

Figure 17 shows the μ_a signal-to-background contrast ratios for the 6 mm deep inclusion phantom as measured using continuous scanning mode. The μ_a value associated with each pixel was divided by the background defined by averaging the μ_a value at 1 x 1 cm regions from the four corners of the image. No smoothing or filtering algorithm was applied to the image. A complete scan of the area yielded 1235 data points and was completed in 4.8 minutes. In comparison, traditional DOSI imaging requires ~20-40 minutes to capture 100-200 data points. The pin holes through the surface of the phantom were visualized as increased absorption and were particularly pronounced at ρ_8.

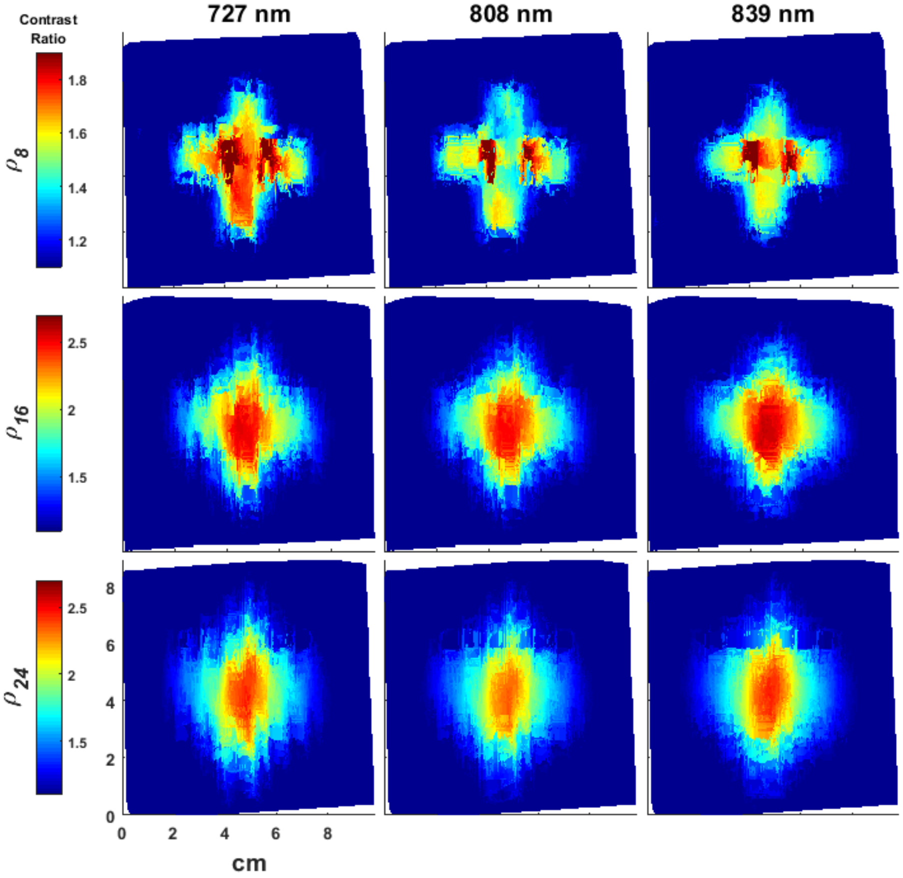

Figure 17: Pixel to background contrast ratio images of the absorption maps. Images were captured by manually raster scanning the surface of the phantom within a 12 x 12 cm defined perimeter. The background was calculated by averaging the data using 1 cm squares at the four corners of the image.

Figure 18 shows the corresponding μ'_s signal-to-background contrast ratios. The contrast ratios were calculated in the same manner as the μ_a contrast ratio maps.

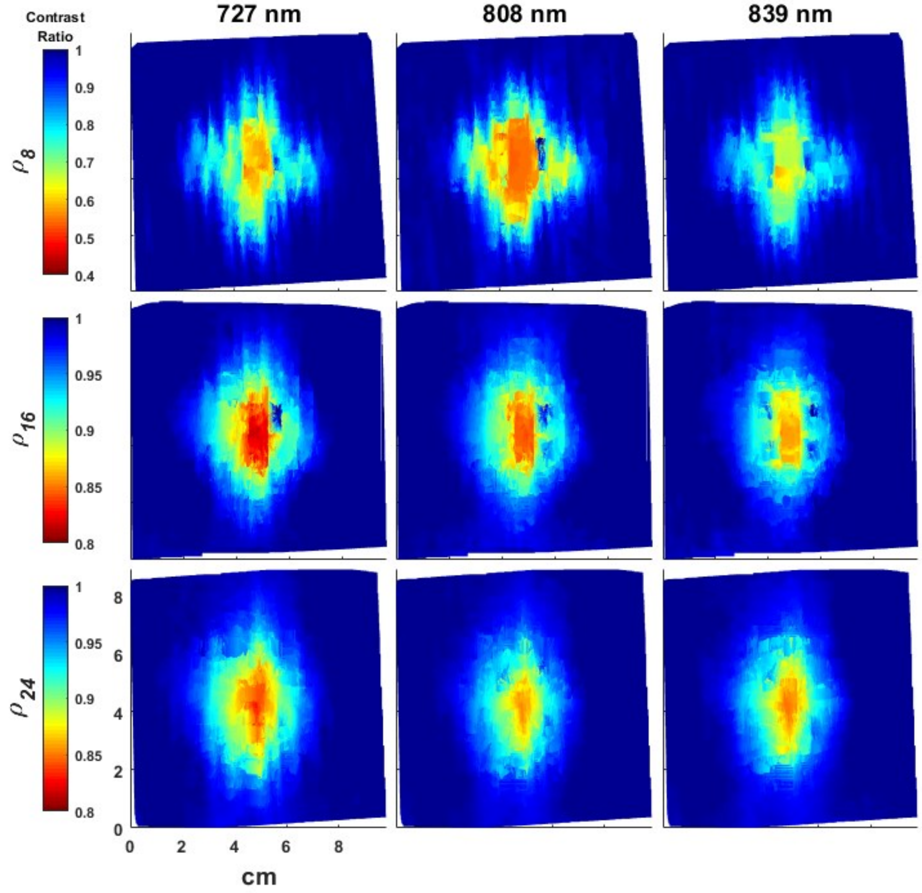

Figure 18: Pixel value to background contrast ratio images of the reduced scattering maps. Absorption and reduced scattering were captured simultaneously within a 12 x 12 cm boundary on the surface of the phantom.

The phantom with the 6 mm deep inclusion was manually imaged an additional time with the probe rotated to an orthogonal orientation. The orthogonal scan roughly followed the same raster scan path. The averaged data using both scan orientations were also calculated. In addition, the data was down sampled to simulate a 1 cm spacing grid spanning 0 to 9 cm. For each coordinate point, the closest data point in the high-density data was sampled. The data were interpolated using a cubic spline method. Data for the 808 nm wavelengths at ρ_8 is shown in fig. 19. Stark differences can be seen in resolution between the data containing the sparse 10 x 10 grid and high-density data generated by continuous scanning.

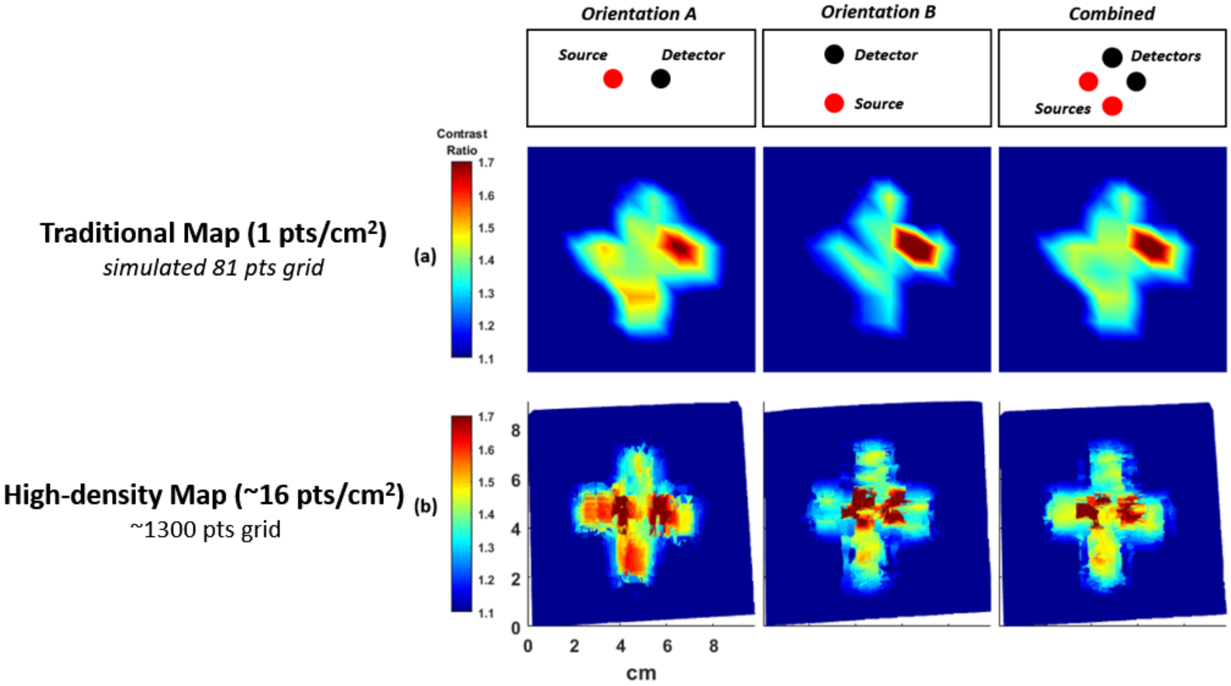

Figure 19: The phantom was imaged twice with the probe at one of two orientations. A third image utilizing an average of the data from the two orthogonal views was generated. Data using the 808 nm wavelength is presented at ρ_8. (a) A grid with simulated 1 cm spacing was calculated. (b) High-density scans of the phantom.

Figure 20 shows the phantom with a 24 mm deep inclusion imaged using shortest and longest SDS (ρ_8 and ρ_{24}) using the same raster-scan method to demonstrate sensitivity to different layers in the heterogeneous phantom. In figure 20a, there is little to no contrast to the imbedded object, while in figure 20b, the object is detected.

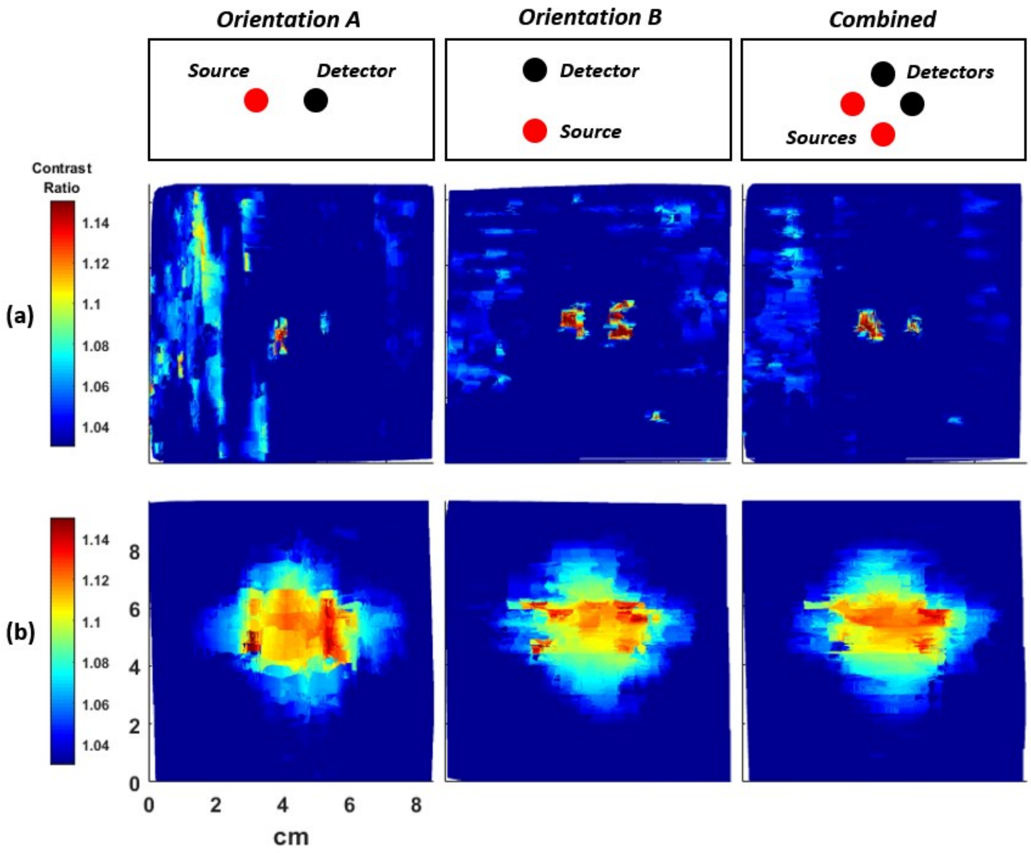

Figure 20: The phantom with a 24 mm deep inclusion was imaged at two source-detector separations and two probe orientations. A final third image was synthesized by averaging the pixel values of data from the two probe orientations. (a) Data presented at the 808 nm wavelength using two probe orientations at ρ_8. The inclusion was not detected in this case. (b) Data presented at the 808 nm wavelength using two probe orientations at ρ_{24}. The inclusion was detected in this case.

3.2. *in vivo Imaging and Hemodynamics*

The calf of a healthy male subject was imaged twice with the probe SDS at either ρ_{10} or ρ_{20}. For each image set, approximately 500 data points were collected over a 5 x 8 cm area in a time span of 2 minutes. Figure 21a shows the perimeter of the imaging area, with a skin-adipose layer thickness of 4.8 mm as seen in the ultrasound image. Figure 21b and 21c shows chromophore maps of *tHb* for ρ_{10} (110.4 ± 14.3 μM) and for ρ_{20}

(126.8 ± 12.4 μM), respectively, taken within the area shown in figure 21a. The Wilcoxon rank sum test showed these two *tHb* distributions were significantly ($p < 0.001$) different (Figure 21d). Similarly, figure 6e and 6f show maps of μ'_s for ρ_{10} and ρ_{20}, respectively. The mean value of each map was 0.63 ± 0.05 mm^{-1} and 0.48 ± 0.03 mm^{-1}, respectively. The Wilcoxon rank sum test showed a significant ($p < 0.001$) difference between the two distributions (Figure 21g). Hemoglobin values as depicted were calculated with consideration of the *FAT* and *H2O* tissue values provided by broadband DOSI. The average tissue *H2O* fraction for ρ_{10} and ρ_{20} was 46.6 ± 3.5% and 48.8 ± 3.7%, respectively, and the average tissue *FAT* fraction was 77.3 ± 5.7% and 66.5 ± 6.2%.

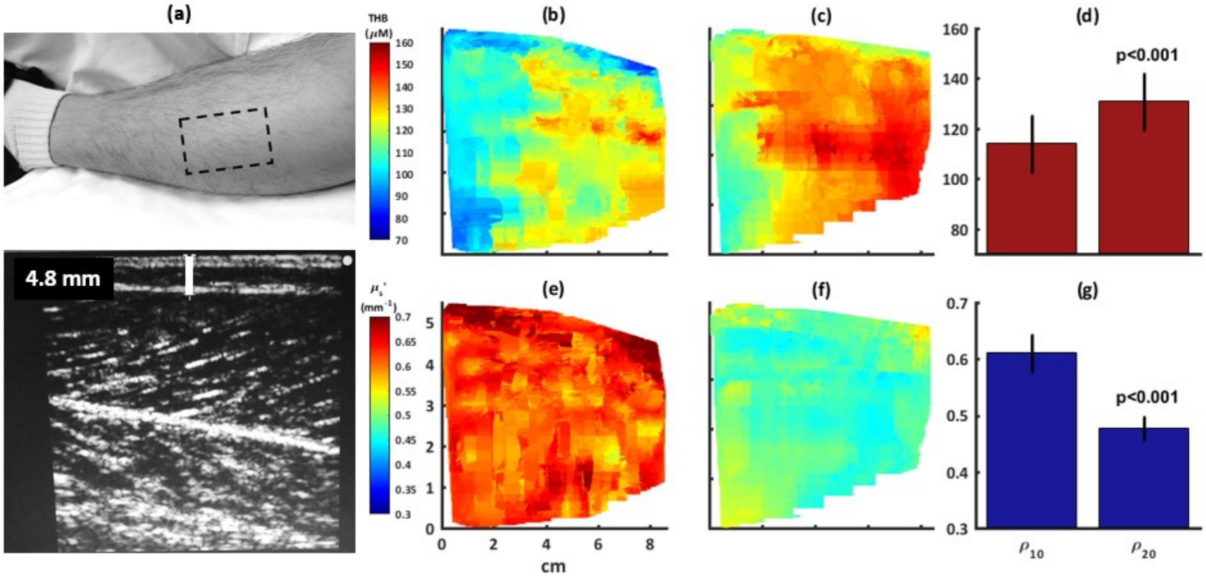

Figure 21: The calf of a healthy male subject was imaged at ρ_{10} and ρ_{20}. (a) The imaging area was approximately 5 x 8 cm. Ultrasound at the center of the imaged area measured a skin-adipose layer of 4.8 mm. (b) *tHb* of the imaged area at ρ_{10} with an average value of 110.4 ± 14.3 μM (c) *tHb* of the imaged area at ρ_{20} with an average value of 126.8 ± 12.4 μM. (d) The mean and standard deviation of *tHb* for ρ_{10} and ρ_{20}. The rank sum test supports that the *tHb* distributions were different ($p<0.001$). (e) μ'_s of the imaged area at ρ_{10} with an average value of 0.63 ± 0.05 mm^{-1} (f) μ'_s of the imaged area at ρ_{10} with an

average value of 0.48 ± 0.03 mm^{-1} (g) The mean and standard deviation of μ'_s for ρ_{10} and ρ_{20}. The rank sum test supports that the μ'_s distributions were different ($p<0.001$).

An arterial occlusion was performed on the calf of the same subject and measured in dual-channel mode asynchronously at ρ_{10} and ρ_{20}. The DOSI measurement was taken at a single spatial location at the center of the imaging area from figure 21a. The overall acquisition frequency was 2 Hz. Figure 22a and 22b show the *HbO2* and *HbR* dynamics for both SDS, respectively. We fit a line through the *HbR* trace during the 90 second occlusion period to calculate the rate of *HbR* accumulation. Figure 22c compares the linear fits between ρ_{10} and ρ_{20}. During the occlusion phase, $\frac{dHbR}{dt}$ at ρ_{10} was 4.26 µM/min and 6.49 µM/min at ρ_{20}.

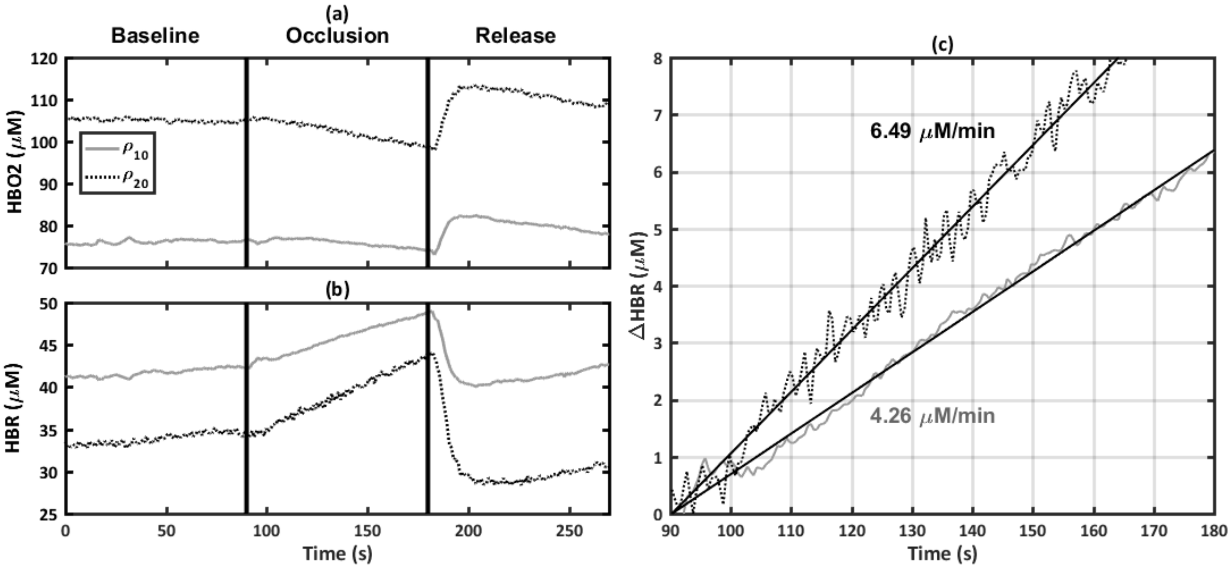

Figure 22: A calf occlusion was performed while measuring ρ_{10} and ρ_{20} in a single probe. (a) *HbO2* dynamics at ρ_{10} (black dashed) and ρ_{20} (gray solid) during 90 seconds of occlusion and release. (b) *HbR* dynamics at ρ_{10} and ρ_{20}. (c) The rate of *HbR* generation was calculated during the 90 second occlusion period.

An occlusion on the thenar of the same subject was performed and measured using the rapid hemodynamics mode at ρ_{24}. The thenar was selected due to the exceptionally thin skin-adipose thickness at this site. The tissue area was assumed to be a single-layer, semi-infinite homogenous medium. DOSI in spectroscopic broadband mode quantified the tissue composition, while CW-NIRS captured rapid hemodynamics. The differential path length factor was calculated using the absolute optical properties[68,72]. The overall data capture speed was 15 Hz. Hemoglobin quantification took into account tissue *H2O* content of 83.8% and a FAT content of 1.2%. Figure 23a shows the *HbO2* and *HbR* dynamics for the occlusion measurement. Figure 23b shows the normalized frequency power spectrum of *HbO2* during baseline and after release in the heartbeat band. The heart rate of the subject was ~1.28 Hz (77 beats per minute) with some small deviation throughout the 4 minute measurement. In addition, the first harmonic of the heart beat can be recognized at 2.46 Hz. Figure 23c shows the tissue oxygen saturation ($StO2 = \frac{HbO2}{THb} \times 100$) and *SaO2* was calculated over time. *rBF* was calculated using the DOSI hemoglobin signal. *rBF* can also be directly measured using DCS provided tissue optical properties from DOSI. Figure 23d compares the calculated *tMRO2* using equation (4) with only parameters recoverable by the DOSI instrument against *tMRO2* calculated using DOSI and DCS parameters. Overall dynamics were similar between the two *tMRO2* measures: higher peak $tMRO_2$ was reported by the DCS (7.9 μM/s) compared to DOSI (5.4 μM/s).

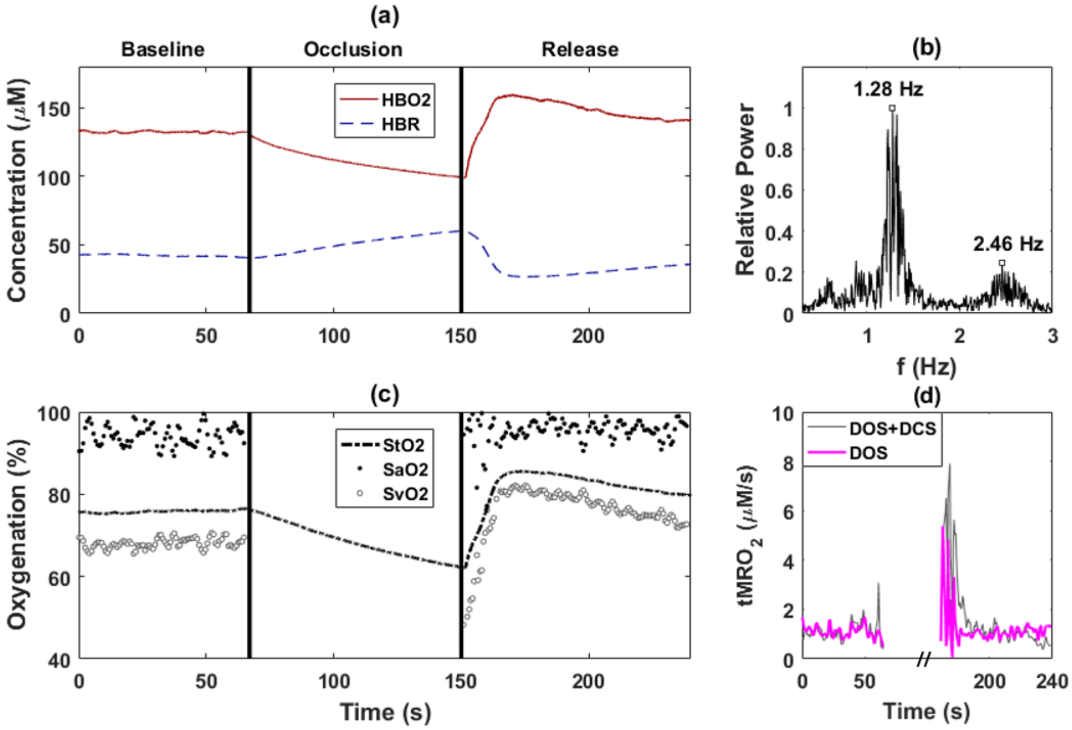

Figure 23: A thenar occlusion was performed on a healthy male subject. (a) *HbO2* (red) and *HbR* (dashed, blue) dynamics are shown. The hemoglobin values were calculated provided *H2O* and *FAT* quantification by broadband DOSI. (b) Normalized frequency power spectrum with a 1.28 Hz peak representing heart rate and a 2.46 Hz peak for the first harmonic of the heart rate (c) *StO2* (dashed), *SaO2* (black dots), and *SvO2* (white circles) was calculated during baseline and release (d) *tMRO2* calculated using DOSI-provided flow (magenta line) and *tMRO2* using DOSI with DCS-provided flow from a secondary occlusion (grey line)

4. Discussion

A high-speed multi-modal DOSI instrument has been demonstrated on optical phantoms and *in vivo* tissues. The different measurement modes can be switched at the user's convenience: 1) full-spectrum broadband mode, 2) continuously scanning imaging mode, 3) dual-channel mode, and 4) rapid hemodynamics mode.

4.1. *Imaging Validation on Optical Phantoms*

To present imaging capabilities of DOSI, a phantom with a 6 mm deep inclusion was continuously scanned using a positionally tracked probe. The shape of the inclusion at ρ_8 was well-defined in the expected shape at all three wavelengths for the μ_a contrast. Some artifacts running vertically throughout the image were observed, but these artifacts can be mitigated by combining data from other probe orientations. The surface holes on the phantom from the pins used to fix the inclusion into place were visualized as heightened attenuation regions for two reasons: 1) diffusive light leakage out of the phantom matrix in these air gaps, 2) coupling loss when the source or detection fiber was scanned directly over a pin hole. The pin holes were clearly visible in the image when scanning at ρ_8. Overestimation of absorption or underestimation of scattering when either the source or detector optical fibers were positioned over the pinholes sometimes resulted in the apparent appearance of four pinholes with certain SDS and wavelength combinations. The ability to distinguish the pinholes within the inclusion region suggests the capability to further delineate small heterogeneities within the structure.

Due to the properties of propagating photons in scattering media, usage of a longer SDS will also effectively increase the average probing depth[73–75]. The result is a more diffuse image with less defined borders, yet with a contrast ratio more closely resembling the contrast ratio given pure samples of the background and inclusion material. Albeit less pronounced, some similar effects can be observed with the μ'_s

contrast. At ρ_{16} and ρ_{24}, the object appears more rounded, and less defined compared to ρ_8. It was noted that the contrast ratio increased with SDS. This may be explained by the probing depth when acquiring data at ρ_8. The average probing depth at ρ_8 may be such that boundary effects at the intersection of the two-layers caused an overestimation of scattering. Longer SDS configurations result in a deeper sampling depth, which effectively minimizes surface effects and renders the measurement volume more homogeneous by fraction. In addition, there may be other scattering factors at the background-inclusion interface such micro-bubbles and small index of refraction mismatches.

The phantom with the 6 mm deep inclusion was also imaged using the probe at two orientations. A third dataset was generated by averaging the absorption map from orientations A and B illustrated in fig. 19. To accentuate the improvement in image resolution using a continuously scanning method, a sparse 1 cm-spaced grid, alluding to traditional DOSI imaging methods, was simulated by digitally selecting points from the denser dataset. This provided the "best-case" scenario for the sparse data. In reality, a manually captured grid will unavoidably have probe placement variation and pixel spacing errors leading to distortion of the imaged object. The four arms of the cross-shaped inclusion could be detected in the sparse data, although with significant aberrations to the object shape. Only one of the two aforementioned pin holes were distinguishable. The undetected pin hole was not sampled due to the sparsity of the 1 cm pixel spacing. In the combined sparse dataset, it was noted that, although there was no discernible resolution enhancement, the contrast dynamic range for interior of the object (sans pin holes) narrowed, as expected of a homogeneous inclusion. The dense data set is depicted in figure 4b. Visually, the cross-shaped object was most clearly defined combining both orientations for the dense data set. To a similar effect in the sparse data set, the reported contrast ratio for the interior of the object was most uniform in the combined case. It was also noted that both of the pin holes were detected using the dense dataset in either orientation. In a clinical setting, data from two or more orientations can be collected using multiple scans. The position for each pixel from one image can be co-registered to the pixels of images from subsequent scans.

For the 24 mm deep inclusion, ρ_8 and ρ_{24} were made the point of comparison using data from the 808 nm wavelength. The same probe orientations (A & B) were utilized to image this phantom. The included object was indistinguishable from the phantom background for either orientation when using imaging at ρ_8. Even when combining the datasets, the inclusion was still undetectable. However, when the phantom was mapped using ρ_{24}, the included object could be detected using probe orientation A and B as shown in fig 20b. At this depth, the diffusive nature of the photon distribution limits the resolution of the image, even when utilizing data from both orientations. However, a non-circular object with 4 distinct protrusions can still be clearly resolved from the ρ_{24} dataset.

4.2. *Dual-Layer In-Vivo Quantitative Composition Imaging and Hemodynamics*

Two-layers of the calf of a healthy male subject was imaged at two SDS. Ultrasound and DOSI in full-spectrum broadband mode measured the skin-adipose thickness and composition, respectively. A survey of the μ'_s and total hemoglobin images, as shown in figure 21 concluded that ρ_{10} and ρ_{20} were probing significantly ($p<0.001$) different tissue compositions. Although true layer separation was not performed, the properties recovered at ρ_{10} was akin to a tissue with higher adipose content than the volume probed at ρ_{20}. This is further corroborated when performing an arterial occlusion of the same tissue site. The hemodynamics were smoothed using a 2nd order median filter as the acquisition speed in this mode was not fast enough to capture pulsatility and evaluation of the overall dynamics was ultimately desired. During the arterial occlusion, there was clear distinction when comparing the deoxygenation rate between the deep and shallow layers; the deeper tissue consumed oxygen 52% faster. This observation reinforces the finding that ρ_{10} and ρ_{20} were probing volumes comparable to adipose and muscle tissue, respectively. Moving forward, due to the ease of capturing multi-modal datasets, it may be advantageous to simply image at multiple SDS on patients (e.g. embedded breast tumors, calf, abdomen) without significantly extending the measurement time.

4.3. *Single-Layer In Vivo Quantitative Pulsatile Hemodynamics*

To demonstrate the rapid-hemodynamic acquisition mode, thenar tissue was measured during an arterial occlusion at ρ_{24} using CW-NIRS with *H2O* and *FAT* fractions of the tissue site quantified using full-spectrum broadband DOSI. Due to the exceptionally sparse skin-adipose thickness in the measurement site, the sampled tissue measured can be approximated as a single homogenous muscle layer. Figure 23c depicts the calculated $StO2$, $SaO2$, and $SvO2$, as provided by equations 1-3. As most of the blood in the human body is reserved in the venous circulatory system, most of the hemoglobin absorption signal originates from venous blood. $SaO2$ was separated from $StO2$ by assuming that pulsatile flow detected by DOSI was dominated by arterial blood flow. By bandpass filtering the hemoglobin data to the heart rate band, pulsatile hemoglobin within the arterial system can be isolated. Using equation (6), rBF can be estimated by use of tHb_{Pulse}. $HbO2_{Pulse}$ may also serve as a surrogate for rBF, but can be affected by the conversion of $HbO2$ to HbR during metabolic activity. tHb_{Pulse} is a more robust estimator of rBF as consumption of HbO_2 is balanced by generation of HbR. Thus, tHb_{Pulse} must directly relate to cardiac output and pulsatile blood flow. Applying (4), $tMRO2$ can be approximated using DOSI parameters. To validate this approach, an additional occlusion was performed and measured using DCS at the same SDS. DOSI optical properties were used for the blood flow calculations. This representative blood flow was also used to calculate $tMRO2$ and compared favorably to the DOSI-only approach. For both methods (DOSI and DOSI+DCS), $tMRO2$ remained relatively steady during baseline, with a small motion artifact observed in the DCS data due to the occlusion cuff inflation. Upon occlusion release, both methods reported a heightened $tMRO2$ due to a sudden influx of blood flow and subsequent repayment of the oxygen debt[76,77]. For the DOSI+DCS system, peak $tMRO2$ was 7.9 μM/s compared to 5.4 μM/s reported by the DOSI approach. This discrepancy can be explained by a variety of factors such as a slight probe placement offset, greater sensitivity of DCS to motion artifacts, or biological variation between the two hyperemic responses. The relaxation of *tMRO2* to baseline in response to the brief 1.5-minute occlusion was approximately 20 seconds for both instruments. These results suggest *tMRO2* dynamics can be approximated using parameters solely provided by DOSI. This approach relies on a DOSI device with sufficient acquisition speed as well as quantified tissue composition using broadband DOSI, further emphasizing the benefits of multiple modalities during a single measurement session.

4.4 *Limitations and Considerations*

In these series of experiments, we have presented an advancement in DOSI by a multi-modal approach with imaging, dual-channel, and rapid single-channel capabilities. However, further improvements can be made for future consideration. The probe-tracking technology based on the HTC Vive requires line-of-sight. This can be mitigated by arranging two or more Lighthouses around the measurement area. In comparison to another probe tracking method[78], Amelard et al. described an camera-based technique to solve probe 3-D position. While this design allows for simultaneous positional tracking, topography generation, and photographic capture, this approach requires lengthy offline image processing. Our method provides 3-D probe position in real-time using consumer grade off-the-shelf parts, but does not automatically co-register images to a topographic map. For future applications, benefits of these two techniques may be combined to provide real-time position, topography, and overlay DOSI chromophore and optical property maps onto 3-D models of scanned areas.

5. Conclusion

We have presented a multi-modal DOSI device capable of broadband spectroscopy, wide-area imaging, dual-channel dual-layer acquisition, and single-channel rapid hemodynamics. The device was demonstrated on tissue-simulating optical phantoms with a buried inclusion as well as *in-vivo*. In comparison to previous iterations of DOSI devices, our device can acquire data at significantly higher speeds, which improves resolution during imaging, and enables monitoring of physiologic changes on a faster timescale. On layered tissue, composition of a mixed-shallow and mixed-deeper layers were recovered, suggesting the constitution of the measured tissues were similar to adipose and muscle, respectively. The enhanced acquisition speed of the presented DOSI device facilitated the recovery of pulsatile hemodynamics, *rBF*, and ultimately *tMRO2* perturbation as a result of arterial occlusion. This was compared against *tMRO2* using *rBF* provided by DCS during a second occlusion. To meet the demands of clinical research, we have developed a flexible, multi-modal DOSI device allowing researchers to expand the scope of data collection capabilities both spatially and temporally.

Disclosures

Dr. Bruce J. Tromberg reports patents, which are owned by the University of California and licensed to commercial entities, that are related to the technology and analysis methods described in this study. This research was completed without their participation, knowledge, or financial support, and data were acquired and processed from patients by coauthors unaffiliated with any commercial entity.

Acknowledgements

This work was supported by the Military Medical Photonics Program AFOSR (FFA9550-17-1-0193), the Leading Foreign Research Institute Recruitment Program through the National Research Foundation of Korea (NRF) funded by the Ministry of Science and ICT (MSIT) (NRF-2018K1A4A3A02060572), and programmatic support from Arnold and Mabel Beckman Foundation.

CHAPTER 4: In-vivo study of hemorrhagic shock and resuscitation

Noninvasive dual-channel broadband diffuse optical spectroscopy of massive hemorrhage and resuscitative endovascular balloon occlusion of the aorta (REBOA) in swine

Jesse H. Lam, Thomas D. O'Sullivan, Tim S. Park, Jae H. Choi, Robert V. Warren, Wen-Pin Chen, Christine E. McLaren, Leopoldo C. Cancio, Andriy I. Batchinsky, and Bruce J. Tromberg

Military Medicine, 183(suppl_1), March 2018, pp 150–156.

Noninvasive dual-channel broadband diffuse optical spectroscopy of massive hemorrhage and resuscitative endovascular balloon occlusion of the aorta (REBOA) in swine

Jesse H. Lam[1], Thomas D. O'Sullivan, PhD[2], Tim S. Park, MD[3], Jae H. Choi, PhD[3],
Robert V. Warren, MS.[1], Wen-Pin Chen, MS.[4], Christine E. McLaren, PhD[4],
Leopoldo C. Cancio, MD[3], Andriy I. Batchinsky, MD[3], Bruce J. Tromberg, PhD[1]

[1]Laser Microbeam and Medical Program, Beckman Laser Institute and Medical Clinic,
University of California, Irvine, 1002 Health Sciences Road, Irvine, CA 92617

[2]Department of Electrical Engineering, University of Notre Dame, 275 Fitzpatrick Hall
Notre Dame, IN 46556

[3]US Army Institute of Surgical Research, 3698 Chambers Pass STE B JBSA FT Sam
Houston, TX 78234

[4]Biostatistics Shared Resource, Chao Family Comprehensive Cancer Center, School of
Medicine, University of California, Irvine, 101 The City Drive Bldg. 23 Route 81 Orange,
CA 92868

Keywords: hemodynamics, oxygenation, hemorrhage, DOS, REBOA

Presentations: Presented as a poster at the 2016 Military Health System Research Symposium (Abstract number: MHSRS-16-0801)

Funding: This research was supported by AFOSR grant award FA9550-14-1-0034 (Advanced Optical Technologies for Defense Trauma and Critical Care). This research was also supported by NIH P41EB015890, the Laser Microbeam and Medical Program (LAMMP), as well as the Arnold and Mabel Beckman Foundation. The animal work was funded by a grant by the Telemedicine and Advanced Technologies Research Center, Fort Detrick, MD, to Pryor Medical, Inc., Arvada, CO; and via a subcontract between Pryor Medical and the Geneva Foundation, Tacoma, WA, for work performed at the U.S. Army Institute of Surgical Research.

Disclaimers: B.J. Tromberg reports patents, which are owned by the University of California, that are related to the technology and analysis methods described in this study. The University of California has licensed diffuse optical spectroscopic imaging technology and analysis methods to Infinit, Inc. This research was completed without Infinit Inc. participation, knowledge, or financial support and data were acquired and processed by coauthors unaffiliated with this entity. The Conflict of Interest Office of the University of California, Irvine, has reviewed both patent and corporate disclosures and did not find any concerns. No potential conflicts of interest were disclosed by the other authors.

Acknowledgements: None

Abstract

Objective: To quantitatively measure tissue composition and hemodynamics during resuscitative endovascular balloon occlusion of the aorta (REBOA) in two tissue compartments using non-invasive two-channel broadband diffuse optical spectroscopy (DOS).

Methods: Tissue concentrations of oxy- and deoxyhemoglobin (HbO2 and HbR), water, and lipid were measured in a porcine model (n=10) of massive hemorrhage (65% total blood volume over 1-hour) and 30-minute REBOA superior and inferior to the aortic balloon.

Results: After hemorrhage, hemoglobin oxygen saturation (StO2 = HbO2 / (HbO2 + HbR)) at both sites decreased significantly (-29.9% and -42.3%, respectively). The DOS measurements correlated with mean arterial pressure (MAP) (R2=0.79, R2=0.88), stroke volume (SV) (R2=0.68, R2=0.88), and heart rate (HR) (R2=0.72, R2=0.88). During REBOA, inferior StO2 continued to decline while superior StO2 peaked 12 minutes after REBOA before decreasing again. Inferior DOS parameters did not associate with MAP, SV, or HR during REBOA

Conclusions: Dual-channel regional tissue DOS measurements can be used to non-invasively track the formation of hemodynamically-distinct tissue compartments during hemorrhage and REBOA. Conventional systemic measures MAP, HR, and SV are uncorrelated with tissue status in inferior (downstream) sites. Multi-compartment DOS may provide a more complete picture of the efficacy of REBOA and similar resuscitation procedures.

Background

Resuscitative endovascular balloon occlusion of the aorta (REBOA) is an emergency resuscitation medical procedure applied in the treatment of severe, non-compressible hemorrhage.[79,80] While initially explored in the 1950's during the Korean War, the procedure has recently regained international interest in both the military and civilian sectors.[81–85] REBOA is a minimally invasive alternative to thoracotomy with aortic clamping, an invasive surgical procedure requiring open-chest access to the aorta.[80,86] The primary rationale behind REBOA is to induce aortic occlusion using an endovascular balloon in order to stop or slow the rate of uncontrollable hemorrhage.[80] In general, a REBOA device is guided up the femoral artery of a patient and then inflated in the aorta. The induced occlusion restores potentially life-saving perfusion to the heart and brain, slows the rate of hemorrhage, and ultimately provides medical practitioners more time to stabilize the patient.[87]

While REBOA is an emerging non-transfusion-based resuscitation technique, assessment of the "two-compartment" REBOA hemodynamics and its effect on tissue oxygenation ($StO2 = \frac{HbO2}{HbO2+HbR}$) and metabolism has yet to be quantified. More specifically, the inflation of an aortic balloon essentially separates the body into two blood volume compartments: 1) upstream from the aortic occlusion, in which blood pressure is restored to critical organs necessary to prolong life; and 2) downstream from the aortic occlusion. Clinical measures obtained invasively, such as mean arterial pressure (MAP) and stroke volume (SV) do not provide complete information about StO2 and metabolism in these two compartments, and they may be inconvenient to use in emergency settings. In contrast, noninvasive broadband diffuse optical spectroscopy (DOS) quickly and easily extracts hemodynamic information based on subsurface tissue chromophore concentrations at multiple sensor locations. Thus, multichannel DOS provides a non-invasive, continuous and quantitative solution to understand hemodynamics and monitor the effectiveness of REBOA.

The DOS technology employed in this study utilizes a combination of four intensity-modulated lasers and continuous wave (CW) broadband light to quantitatively measure tissue near-infrared absorption and reduced scattering spectra spanning from 650-1000nm.[1,5] Tissue concentrations of oxyhemoglobin (HbO_2,), deoxyhemoglobin (HbR), water (H_2O) and lipid (FAT) are derived[1] from broadband absorption spectra. Unlike conventional near-infrared spectroscopy (NIRS), broadband DOS directly measures tissue optical scattering, as well as water and lipid concentrations to provide accurate quantification of tissue chromophores. Previous preclinical studies have shown that broadband DOS is sensitive to hemoglobin and StO2 levels during hemorrhagic shock and transfusion-based resuscitations.[55,54]

In this study, we apply a two-channel broadband DOS instrument to assess tissue hemodynamics in a swine model of severe hemorrhage and REBOA resuscitation. Typical systemic parameters, namely, MAP, SV, and HR are contrasted with regional DOS parameters.

Methods

This analysis involved a subset (N=17) of male Sinclair miniature swine (Sinclair Bio Resources, MO, USA), weighing 37±7 kg, that were involved in a larger (N=35) study of massive hemorrhage and resuscitation.[81] Seven subjects were excluded due to: low signal-to-noise ratio (SNR) (N=3), absent data at critical time points such as baseline (N=2), and unusually low baseline HbO_2 values below 1 μM (N=2), resulting in 10 analyzable subjects. Low SNR and total hemoglobin values were likely due to variations in probe placement on Sinclair swine, which have thick avascular subcutaneous tissue. The study was approved by the U.S. Army Institute of Surgical Research Animal Care and Use Committee (protocol number A-14-002). It was conducted in compliance with the Animal Welfare Act and the implementing Animal Welfare Regulations, and in accordance with the principles of the *Guide for the Care and Use of Laboratory Animals*. It was performed at a facility accredited by AAALAC International.

Surgical procedures are described in greater detail in Park et al.[81] Briefly, the swine were anesthetized, and then monitored using an anesthesia machine (Dräger Fabius GS, Dräger Medical Inc., PA, USA). The animal was then placed in a custom sling, allowing it to rest in an anatomic quadruped position. Controlled hemorrhage was achieved using a programmable peristaltic pump (Masterflex, Cole-Parmer, IL, USA). Blood was recovered from the animal into blood collection bags. The blood-collection bags rested on a digital scale in order to provide a metric on the amount of fluid removed. The hemorrhage consisted of 65% total-blood-volume (TBV) hemorrhage over 60 minutes, where TBV was estimated as 65 ml/kg. The hemorrhage rate was approximately exponential, with the target values listed in Table 2.

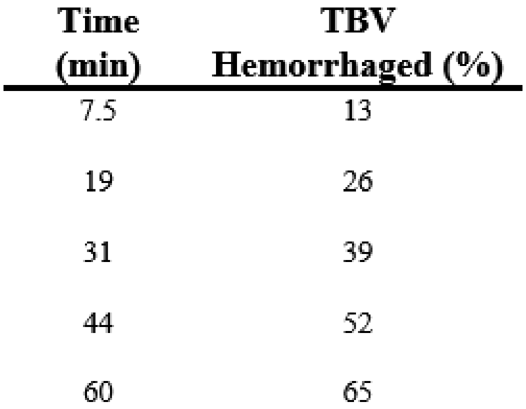

Time (min)	TBV Hemorrhaged (%)
7.5	13
19	26
31	39
44	52
60	65

Table 2: Targeted blood loss volumes for the controlled hemorrhage period. Blood was drawn from each animal using a peristaltic pump. By 60 minutes, approximately 65% of total blood volume was removed from each subject.

After the hemorrhage period, the peristaltic pump was stopped. Immediately following, the REBOA device was introduced via the common femoral artery and placed between the subclavian and the celiac arteries (aortic zone 1).[87] The endovascular device utilized was an investigational catheter (ER-REBOA, Pryor Medical, Inc., TX, USA) designed specifically for REBOA applications. After device placement, the balloon was inflated for 30 minutes using 8 ml of saline solution. Successful occlusion was confirmed by arterial blood pressure dropping to near 0 downstream from the occlusion. Balloon placement was also verified after the experiment by computed tomography and necropsy. A high-pressure monitoring line (Smith Medical ASD INC., OH, USA) was used with an Infinity HemoMed Pod (Dräger Medical Inc., Schleswig-Holstein, Germany) for arterial-blood-pressure measurements. An EKG device

(Osypka Medical Inc., CA, USA) was used to record heart rate. Sensor data was averaged over 6 minutes.

Optical measurements were collected with a broadband, dual-channel DOS research device (Beckman Laser Institute, University of California, Irvine, CA, USA). A custom plastic fiber-coupled probe with a source-detector separation distance of 20 mm was secured to the neck (DOS channel 1) and ham (DOS channel 2) of the subjects using sutures, as shown in Figure 24. Measurements were taken approximately every 15 seconds, and 6-minute block averages are presented in this report.

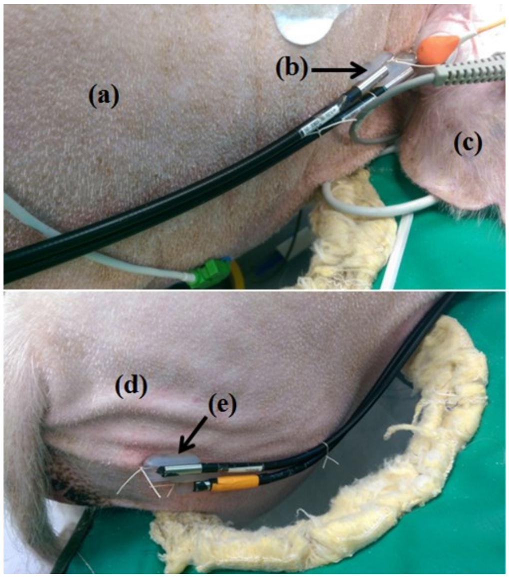

Figure 24: Location of the measurement sites shown (a) neck (b) DOS channel 1 probe (c) ear (d) ham (e) DOS channel 2 probe.

The technology behind the DOS instrument has been extensively detailed in previous studies.[1,5,88] Briefly, the device contains a frequency-domain photon migration (FDPM) component consisting of four discrete wavelength sources (660, 690, 785, and 830 nm laser diodes, 20mW average optical power) and an avalanche photodiode module (C5658 module with S6045-03 photodetector, Hamamatsu, Japan). The broadband steady-state component consists of a tungsten-halogen broadband source (Ocean Optics HL-2000, FL, USA) and spectrometer (AvaSpec-ULS2048X64-USB2, Apeldoorn, Netherlands). Fiber bundles deliver and collect the light to/from the tissue. After calibration by use of a reference optical phantom, the FDPM amplitude and phase are fit using the P_1 diffusion approximation to the radiative transport equation in order to recover the absorption (μ_a) and reduced scattering (μ_s') coefficients for each laser diode wavelength.[15,26] The broadband state-state reflectance spectrum is calibrated with a reflectance standard (Labsphere Inc., NH, USA). The μ_s' is recovered across the near-infrared wavelength range by fitting μ_s' values from the FDPM component of the DOS device to a power law, $\mu_s'(\lambda) = A\lambda^{-B}$, in which A is the scatter amplitude, λ is the wavelength, and B is the scattering slope.[1,89,11]

Total data-acquisition time including both the frequency-domain and steady-state component is typically under 5 seconds. Chromophore concentrations are calculated by performing a least-squares minimization including HbO_2, HbR, H_2O, and FAT to the broadband near-infrared absorption spectrum. In addition, a spectrally flat baseline offset was included in the fit, which has been shown to improve the chromophore fits for broadband DOS devices.[90] Additional indices are derived from these parameters, including total hemoglobin (THC = HbO_2 + HbR) and StO2.

Because of the correlation in the percentage change from baseline across measurement times, generalized estimating equations (GEE) analyses were performed for DOS parameters, with a normal link function and an exchangeable working matrix.

From GEE models, the estimated mean and standard error of the percentage change from baseline was obtained and used to construct scatter plots.

Linear regression analysis was performed in which the data for the 10 subjects were averaged for each time point. The mean and standard error for baseline DOS parameters were calculated for each channel. The coefficient of determination (R^2) and p-value was estimated using the MATLAB "corr" function as a measure of the linear relationship between DOS and systemic parameters.

Results

Baseline DOS parameters for each channel before hemorrhage are shown in Table 3. Recovered "A" and "B" parameters from the scattering power law in equation (1) are also provided. We note the relatively low StO_2 at these tissue sites in the Sinclair model, likely due to the relatively low perfusion and total hemoglobin content in their thick fatty subcutaneous tissue (HbO_2 = 7 and 8 μM, FAT% = 33 and 45; neck and ham, respectively).

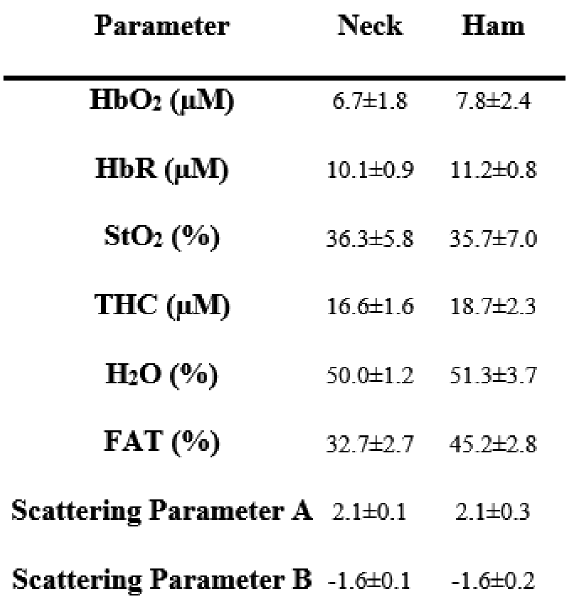

Parameter	Neck	Ham
HbO_2 (µM)	6.7±1.8	7.8±2.4
HbR (µM)	10.1±0.9	11.2±0.8
StO_2 (%)	36.3±5.8	35.7±7.0
THC (µM)	16.6±1.6	18.7±2.3
H_2O (%)	50.0±1.2	51.3±3.7
FAT (%)	32.7±2.7	45.2±2.8
Scattering Parameter A	2.1±0.1	2.1±0.3
Scattering Parameter B	-1.6±0.1	-1.6±0.2

Table 3. Tabulated absolute quantities from neck (channel 1) and ham (channel 2) of the diffuse optical spectroscopy instrument at baseline are shown. Recovered "A" and "B" parameters from the scattering power law in equation (1) are also provided. The baseline for each subject was defined as a 6-minute average prior to the start of hemorrhage. Errors are reported as standard error.

Time-varying DOS parameters and standard cardiac measures (MAP, HR, and SV) from the GEE model during hemorrhage and REBOA are shown in Figure 25. Because of subject-to-subject variation in baseline DOS values, the data are presented as percent change from baseline values. The total experiment duration was 90 minutes, described by three major events: baseline at 0 minutes, hemorrhage until 60-minute mark, and REBOA between the 60- and 90- minute marks. For all subjects, channel 1 measured upstream from the occlusion (neck), while channel 2 measured downstream (ham).

Hemodynamic trends are shown in Figure 25a. The mean difference between the two DOS channels was calculated using a GEE model. Red asterisks are used to denote when the difference between channels was statistically significant (i.e., the 95% confidence interval of the mean differences did not cross the zero value). In both measurement sites HbO_2 and StO_2, which are reflective of tissue microvascular perfusion and metabolism, respectively, decreased during hemorrhage while HbR increased. This is consistent with increased oxygen extraction accompanying diminished perfusion during hemorrhage. The HbR increased rapidly in the ham region, and then leveled off to match the change in the neck region by the end of the hemorrhage period. During REBOA HbO_2 increased in the neck, while it continued to decrease in the ham. The HbR increased significantly in the ham during REBOA from minutes 72 until 84. By the end of the REBOA, HbO_2, HbR, and StO_2 in both channels converged and no longer remained significantly different.

In Figure 25b, bulk tissue H_2O, FAT, and THC trends are displayed. For the majority of the experiment, H_2O, FAT and THC remained within a few percent from baseline. No significant difference was observed between channels for most time points. However, broadband DOS characterization of H_2O and FAT composition played an important role in the ability of DOS to accurately assess hemodynamics due to the relatively high fat and low hemoglobin levels in the skin of the Sinclair swine model.

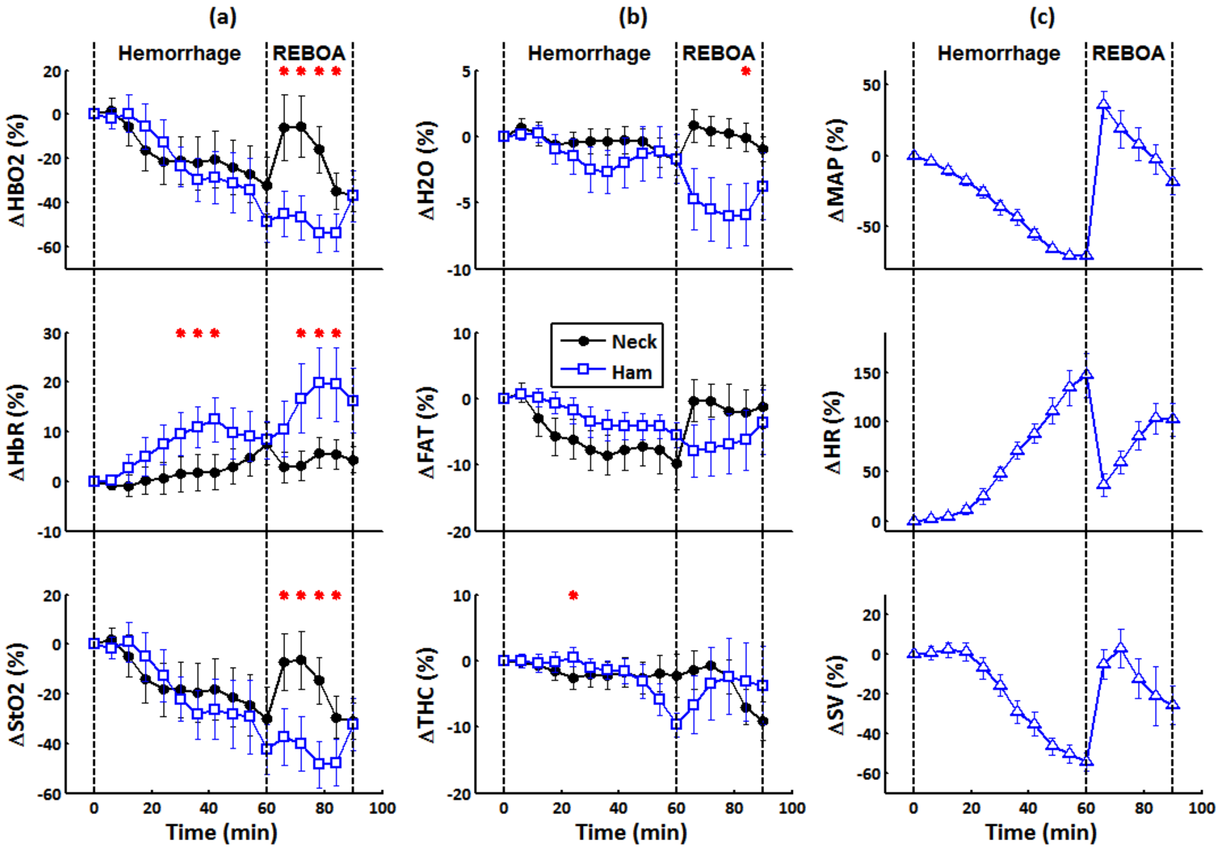

Figure 25: Diffuse optical spectroscopy (DOS) and cardiac parameters from a generalized estimating equations model over time. Hemorrhage occurred from 0-60 minutes followed by REBOA at 60-90 mins. For all animals, channel 1 measured upstream from the aortic occlusion site (neck), while channel 2 measured downstream (ham). Each time point is an average of 6 minutes of data and is presented as the percent change from its baseline value. Significant difference between channels is denoted by a red asterisk (*). **(a)** Hemodynamic trends HbO_2, HbR, and StO_2 from the dual-channel DOS device **(b)** H_2O, FAT and THC tissue parameters from the dual-channel DOS device **(c)** MAP, HR, and SV systemic parameters from various clinical instruments.

Typical cardiac parameters are shown Figure 25c. During hemorrhage, MAP and SV deteriorated while HR increased. During REBOA, MAP and SV exhibited a sudden increase after inflation of the aortic balloon. However, as the aortic balloon remained inflated, MAP and SV began to decrease below baseline values, but stayed above end-hemorrhage levels. Heart rate responded in similar, but opposite trends, showing a decline soon after REBOA inflation, but increased as REBOA was maintained.

Linear regression analysis was performed comparing HbO_2 to MAP and SV as shown in Figure 26a and 26b for the neck and ham region, respectively. Data for the 10 subjects was averaged at each time point for each channel. Coefficients of determination (R^2) and p-values characterizing the linear relationship between DOS and cardiac parameters were calculated. During the hemorrhage, HbO_2 was strongly associated with MAP in neck (R^2=0.76, P=0.001) as well as ham regions (R^2=0.89, P<0.001). During REBOA, neck HbO_2 remained correlated with MAP (R^2=0.83, P=0.03), while ham HbO_2 was no longer associated (R^2=0.06, P=0.70). Similar associations observed between HbO_2 and SV. The HbO_2 and SV were correlated in both measurement sites during hemorrhage (neck R^2=0.65, P=0.01; ham R^2=0.90, P<0.001), but only in neck during REBOA (neck: R^2=0.92, P=0.01; ham: R^2=0.03, P=0.77).

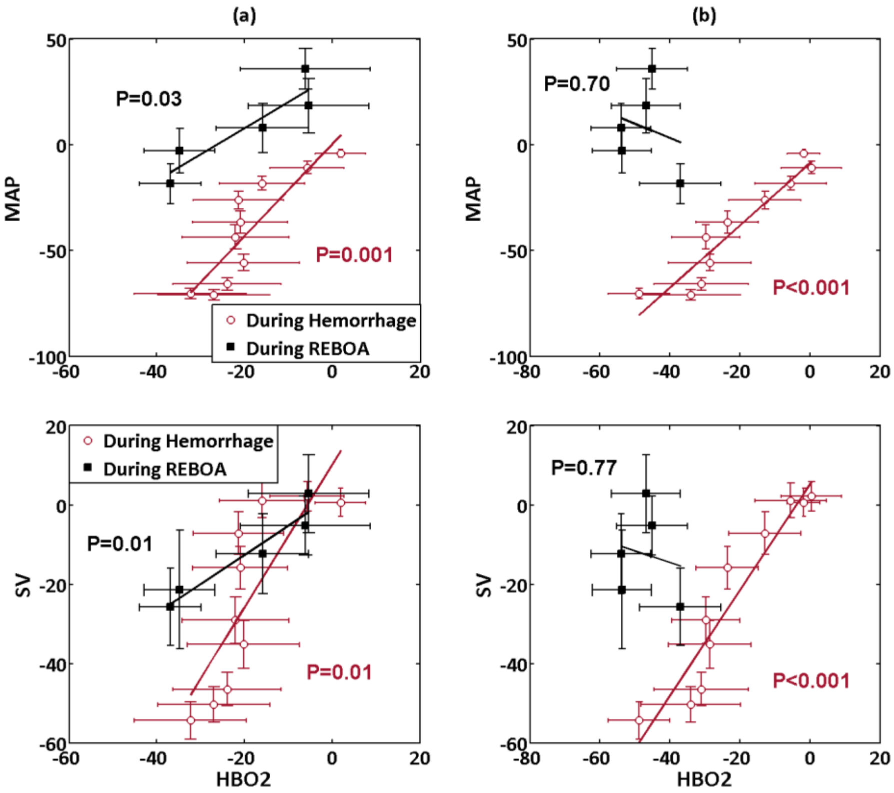

Figure 26: Linear regression analysis of HbO_2 with systemic parameters SV and MAP. **(a)** Neck HbO_2 is significantly associated with MAP and SV during the hemorrhage and maintains significance during REBOA **(b)** Ham HbO_2 is highly correlated with MAP and SV during hemorrhage, but loses significant association during REBOA.

Table 4 further details the coefficients of determination relating DOS and cardiac parameters. During hemorrhage, all DOS parameters are associated ($P<0.05$) with cardiac parameters in both channels. During REBOA, HbO_2 and StO_2 remained associated with all systemic parameters in channel 1. For channel 2, no associations with cardiac parameters were observed.

Channel 1 Coefficients of Determination (R^2)

	Hemorrhage			REBOA		
	MAP	**HR**	**SV**	**MAP**	**HR**	**SV**
HbO_2	0.76*	0.69*	0.65*	0.83*	0.82*	**0.92***
HbR	0.79*	0.88*	0.82*	0.40	0.69	0.43
StO2	0.79*	0.72*	0.68*	0.82*	0.82*	**0.92***

Channel 2 Coefficients of Determination (R^2)

	Hemorrhage			REBOA		
	MAP	**HR**	**SV**	**MAP**	**HR**	**SV**
HbO_2	0.89*	**0.91***	**0.90***	0.06	0.01	0.03
HbR	0.61*	0.46*	0.49*	0.38	0.62	0.14
StO_2	0.88*	0.88*	0.88*	0.01	0.06	0.00

Table 4. Diffuse optical spectroscopy (DOS) Channel 1 (top) and Channel 2 (bottom) coefficients of determination for all 10 subjects. During REBOA, DOS parameters in Channel 1 associate with systemic parameters while Channel 2 is not. The asterisk (*) is used to denote if the relationship is statistically significant ($P<0.05$). Cases with high coefficients of determination ($R^2>0.90$) are displayed as bolded text.

Discussion

There has been much interest in assessing the potential of REBOA to replace thoracotomy with aortic clamping as a minimally invasive approach to treat non-compressible hemorrhage.[79–85] In previous work we were able to assess the efficacy of transfusion-based resuscitation using a single channel DOS that monitored systemic hemoglobin levels with a non-invasive probe.[28,55] However, REBOA necessitates occlusion of the aorta, and thus, the subsequent creation of two distinct blood volume compartments: an upstream compartment, and a downstream compartment. Accordingly, in this study we employ a dual-channel DOS instrument in order to follow regional tissue hemodynamics from two different blood volume compartments in a model of massive hemorrhage and REBOA.

Baseline concentrations of HbO_2, HbR, StO2, THC, and H_2O were similar at each measurement site, while FAT levels were slightly elevated in the ham region. However, because of the thick sub-cutaneous fat layer of the swine model, we observed relatively high overall FAT% and low THC at baseline. This is consistent with a previous study[30] which reported a similar adipose composition measured in humans as well as our own observations (data not shown) of resected skin showing up to 2 cm-thick adipose in the ham region. Under these conditions, the ability of broadband DOS utilizing hundreds of optical wavelengths to quantitatively measure all major tissue components can improve sensitivity to hemodynamics during hemorrhage and REBOA.

During the hemorrhage period, the resulting HbO_2, HbR and StO_2 trends were as expected for a blood loss model: HbO_2, and StO_2 decreased over time, while HbR remained elevated from baseline. This is indicative of hemorrhage-induced reductions in microvascular perfusion accompanied by an increase in tissue oxygen extraction. No significant difference was observed between neck and ham in the rate of HbO_2 and StO_2 decrease during hemorrhage. The values for HbR in the neck were significantly different from the ham for a period of 18 minutes as seen in Figure 2a. However, by the end of the hemorrhage period, HbR trends in both channels were no longer statistically different. This temporary divergence in HbR may have been the result of initially different metabolic rates of the two underlying tissue sites. Overall, DOS and conventionally-measured systemic parameters (MAP, HR, and SV) were significantly correlated in both channels between during the hemorrhage period, as shown in Table 3. These results indicate that both DOS channels were capable of tracking hemorrhage with similar performance to invasively obtained systemic parameters.

During REBOA, significant differences between DOS channels were observed for HbO_2 and StO_2 between 66 to 84 minutes as seen in Figure 2a; differences were also observed between 72 to 84 minutes for HbR. This observation is explained by the fact that the neck channel interrogated an area in which blood pressure was restored as a result of REBOA inflation, while the ham channel probed a region in which no intervention was provided. In other words, two blood volume compartments with unique hemodynamics were formed as a direct consequence of the aortic occlusion. Two measurement sites, and thus, two-channel systems are recommended for investigating REBOA models.

During severe hemorrhage, loss of blood volume leads to a reduction of systemic blood pressure. Under these conditions, HR increases in an attempt to compensate for reduced SV to meet tissue metabolic demands. Throughout the hemorrhage period, DOS parameters in both channels were significantly correlated with systemic parameters as presented in Table 3. However, upon REBOA inflation, the DOS channel measuring downstream (ham) from the occlusion loses all association with systemic parameters. This clear discrepancy between systemic and tissue-level assessments suggests that conventional metrics such as MAP, HR and SV cannot used to characterize the impact of REBOA on downstream tissue viability. In contrast, as shown in Figure 2a, despite isolation from blood flow, DOS recovers hemodynamics as well as tissue status in this region. Thus, during hemorrhage, two-channel DOS tracks conventional systemic parameters and during REBOA, DOS can provide additional information this is not available systemically. One potential application of these findings is studying standard REBOA procedures, such as the length and degree of occlusion. Maximizing survival rates while minimizing harmful physiological consequences of ischemia is desirable, but remains challenging.[82,91]

Several limitations can be identified in this study. While DOS is capable of recovering tissue hemoglobin and oxygenation status, the highly scattering nature of light propagation in skin and the 2 cm source-detector separation of our DOS probe limits the mean interrogation depth to ~6-9 mm for typical 2 cm thick tissues.[92] While this is sufficient for recovering subsurface microvascular hemodynamics, deeper organ status cannot be evaluated non-invasively. We also utilized Sinclair swine subjects with variably-thick, low-blood-volume, fatty, skin. In addition, fiber coupling inefficiencies with light sources as well as detector components resulted in lower-than-expected DOS signal-to-noise ratios (SNR). Finally, the effect of anesthesia on hemodynamic responses is difficult to quantify.

The results of this study demonstrate the feasibility of a non-invasive, two-channel DOS device to assess hemodynamics in different tissue regions during hemorrhage and REBOA-induced resuscitation. Highly correlated relationships between DOS and systemic parameters were seen during hemorrhage and maintained during REBOA upstream of the aortic occlusion. Downstream of the occlusion, systemic MAP, HR, and SV are uncorrelated with tissue status while DOS maintains sensitivity to regional changes in tissue perfusion and metabolism. We conclude that dual-channel DOS measurements of regional tissue perfusion and metabolism can be used successfully to non-invasively track the formation of hemodynamically-distinct tissue compartments during hemorrhage and REBOA resuscitation. Because conventional systemic measures (MAP, HR, SV) correlate with DOS upstream of REBOA but do not provide information on downstream tissue status, multi-compartment non-invasive DOS monitoring may provide a more complete picture of the efficacy of REBOA and similar resuscitation procedures.

CHAPTER 5: Conclusion and recommended future work

In this dissertation, I characterized a clinical DOSI device on optical phantoms and an *in-vivo* breast imaging. The clinical DOSI device was used for a variety of prior mentioned studies. However, this clinical DOSI device was not without limitations; greater instrument flexibility and additional modalities were desired. I demonstrated the value of such a multi-modal DOSI system to capture multi-modal data. I showed that in a single instrument, one can quickly access different layers of tissue including high-resolution chromophore and optical property maps, dual-layer hemodynamics, pulsatile hemodynamics, and broadband spectroscopic analysis. In addition, I presented data in a swine study using multi-channel DOSI. This further demonstrated the value of having access to multi-channel data. A multi-modal DOSI device provides clinicians and researchers more tools to understand the physiology and potentially diseases being studied.

Moving towards future advancement of DOSI technology, I recommend additional work to miniaturize DOSI device to form-factors suitable for portable applications. Dr. Yazdi[93] in his capstone PhD dissertation project designed an application-specific integrated circuit as a millimeter-scale network-analyzer replacement for performing FDPM (FD-ASIC)[93]. The FD-ASIC and comparison to other network analyzer solutions is shown in figure 27.

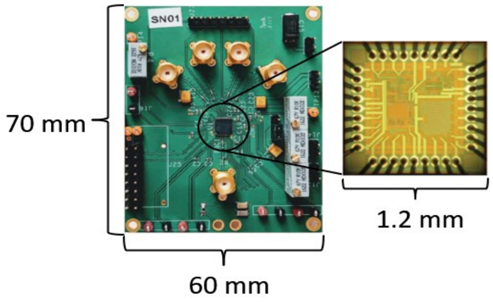

	MDOSI	Sthalekar et al.	FD-ASIC
Size	57600 mm^3	3.2 mm^3	1.5 mm^3
Modulation Range	50-500 MHz	100 MHz	50-1000 MHz
Power draw	7.5 W	0.020 W	0.100 W

Figure 27: The FDPM ASIC represents the first step to miniaturize DOSI to a handheld and wearable form-factor[93]. Compared to other solutions[5,94], the ASIC has greater modulation range while maintaining a smaller size.

Part of my role in this project was designing and testing of a complementary compact laser diode driver (LDD) circuit to drive a 6-to-1 laser beam combiner[95]. The circuit board layout is shown in figure 28 and the results of optical output stability tests are shown in figure 29. The LDD circuit measures 2.5 x 3.5 inches.

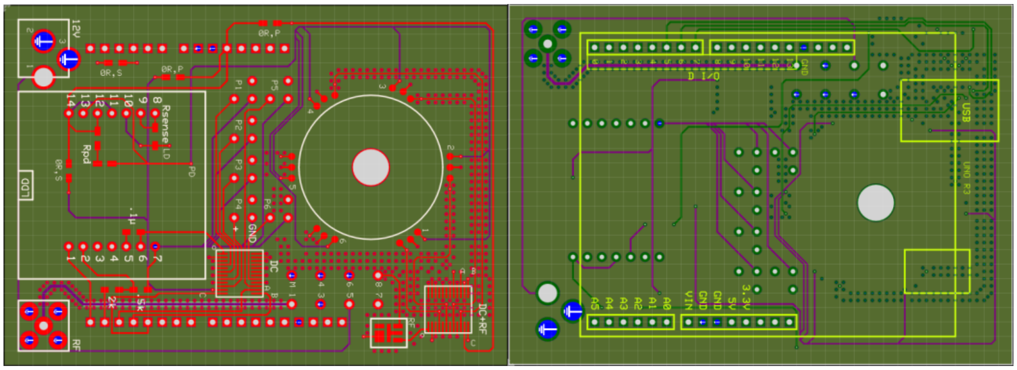

Figure 28: Front (left) and back (right) side of the prototype laser diode board to power a 6-to-1 laser beam combiner[95] controlled by an Arduino Uno R3. The approximate board size is 2.5 x 3.5 inches. Red traces refer to top layer copper, dark green is the bottom layer copper, blue is the 2nd layer copper, purple is the 3rd layer copper, white is the top silkscreen layer, and yellow is the bottom layer silkscreen.

Compared to the MDOSI LDD, the custom LDD solution had better optical stability over the test duration (60 minutes). However, it should be noted that the MDOSI LDD also had excellent optical stability (<1% standard deviation). Larger, low-frequency fluctuations were likely due to the ambient air conditioning.

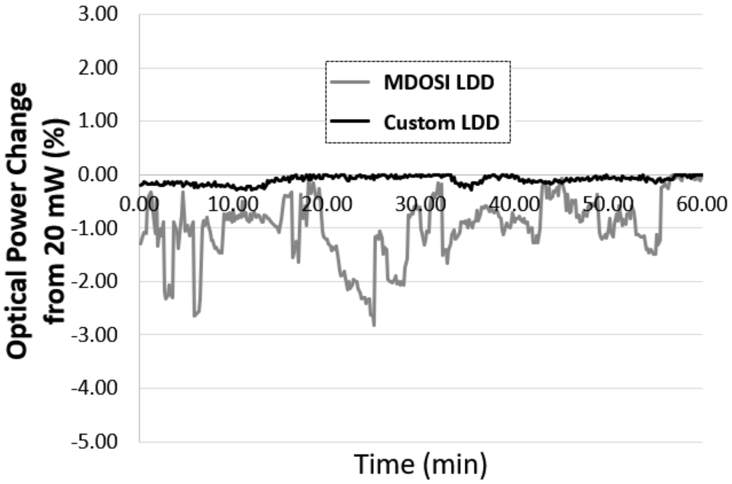

Figure 29: Optical output stability of the custom LDD over time compared to the MDOSI laser driver. The test was conducted using the 730 nm laser diode on the custom LDD while the MDOSI utilized the 785 nm laser diode. The custom LDD board had the most stable optical output over the course of the experiment, based on standard deviation.

Although work on developing the FD-ASIC for Biophotonics applications is still on-going, the FD-ASIC foreshadows the next generation of DOSI devices as a portable platform. Wearable, quantitative, spectroscopic devices have the potential to fundamentally change our practices when monitoring dynamic physiology. This can impact areas such as sports medicine, civilian trauma care, military medicine, and other unexplored areas not yet enabled by such portability. For continuing efforts in this area, I advise focusing on integration of the FD-ASIC into wearable device with smaller, lower-power light sources, such as vertical cavity surface-emitting lasers, and low-power detectors, such as silicon photomultipliers.

BIBLIOGRAPHY

1. Bevilacqua F, Berger AJ, Cerussi AE, Jakubowski D, Tromberg BJ. Broadband absorption spectroscopy in turbid media by combined frequency-domain and steady-state methods. *Appl Opt*. 2000;39(34):6498-6507. doi:10.1364/AO.39.006498

2. Jubran A. Pulse oximetry Amal Jubran. *Crit Care*. 1999;3:11-17.

3. Sinex JE. Pulse oximetry: Principles and limitations. *Am J Emerg Med*. 1999;17(1):59-66. doi:10.1016/S0735-6757(99)90019-0

4. No KS, Chou PH. Mini-FDPM and heterodyne mini-FDPM: Handheld non-invasive breast cancer detectors based on frequency-domain photon migration. *IEEE Trans Circuits Syst I Regul Pap*. 2005;52(12):2672-2685. doi:10.1109/TCSI.2005.857927

5. No K-S, Kwong R, Chou PH, Cerussi A. Design and testing of a miniature broadband frequency domain photon migration instrument. *J Biomed Opt*. 2009;13(5):050509. doi:10.1117/1.2998473

6. Leproux A, Kim YM, Min JW, et al. Differential diagnosis of breast masses in South Korean premenopausal women using diffuse optical spectroscopic imaging. *J Biomed Opt*. 2016;21(7):074001. doi:10.1117/1.jbo.21.7.074001

7. Jacques SL. Optical properties of biological tissues: A review. *Phys Med Biol*. 2013;58(11). doi:10.1088/0031-9155/58/11/R37

8. Cheong WF, Prahl SA, Welch AJ. A review of the optical properties of biological tissues. *IEEE J Quantum Electron*. 1990;26(12):2166-2185. doi:10.1109/3.64354

9. Steiner R. Laser-Tissue Interactions. In: *Laser and IPL Technology in Dermatology and Aesthetic Medicine*. Berlin, Heidelberg: Springer Berlin Heidelberg; 2011:23-36. doi:10.1007/978-3-642-03438-1_2

10. Schmitt JM, Kumar G. Optical scattering properties of soft tissue: a discrete particle model. *Appl Opt*. 1998;37(13):2788. doi:10.1364/AO.37.002788

11. Mourant JR, Fuselier T, Boyer J, Johnson TM, Bigio IJ. Predictions and measurements of scattering and absorption over broad wavelength ranges in tissue phantoms. *Appl Opt*. 1997;36(4):949. doi:10.1364/AO.36.000949

12. Haskell RC, Svaasand LO, Tsay TT, Feng TC, McAdams MS, Tromberg BJ. Boundary conditions for the diffusion equation in radiative transfer. *J Opt Soc Am A Opt Image Sci Vis*. 1994;11(10):2727-2741. doi:10.1364/JOSAA.11.002727

13. Pogue BW, Patterson MS. Frequency-domain optical absorption spectroscopy of finite tissue volumes using diffusion theory. *Phys Med Biol*. 1994;39(7):1157-1180. doi:10.1088/0031-9155/39/7/008

14. Fishkin JB, Coquoz O, Anderson ER, Brenner M, Tromberg BJ. Frequency-domain photon migration measurements of normal and malignant tissue optical properties in a human subject. *Appl Opt*. 1997;36(1):10-20. doi:42829 [pii]

15. Pham TH, Coquoz O, Fishkin JB, Anderson E, Tromberg BJ. Broad bandwidth frequency domain instrument for quantitative tissue optical spectroscopy. *Rev Sci Instrum*. 2000;71(6):2500. doi:10.1063/1.1150665

16. Jacques SL, Pogue BW. Tutorial on diffuse light transport. *J Biomed Opt*. 2008;13(4):041302. doi:10.1117/1.2967535

17. Testorf M, Österberg U, Pogue B, Paulsen K. Sampling of time- and frequency-domain signals in Monte Carlo simulations of photon migration. *Appl Opt*. 1999;38(1):236. doi:10.1364/AO.38.000236

18. Alexandrakis G, Farrell TJ, Patterson MS. Monte Carlo diffusion hybrid model for photon migration in a two-layer turbid medium in the frequency domain. *Appl Opt*. 2000;39(13):2235. doi:10.1364/ao.39.002235

19. Haskell RC, Svaasand LO, Tsay T-T, Feng T-C, Tromberg BJ, McAdams MS. Boundary conditions for the diffusion equation in radiative transfer. *J Opt Soc Am A*. 1994;11(10):2727. doi:10.1364/JOSAA.11.002727

20. Fantini S, Sassaroli A. Frequency-Domain Techniques for Tissue Spectroscopy and Imaging. In: *Handbook of Optical Biomedical Diagnostics, Second Edition, Volume 1: Light-Tissue Interaction*. SPIE PRESS; :1-52. doi:10.1117/3.2219603.ch7

21. Patterson MS, Moulton JD, Wilson BC, Berndt KW, Lakowicz JR. Frequency-domain reflectance for the determination of the scattering and absorption properties of tissue. *Appl Opt*. 1991;30(31):4474. doi:10.1364/AO.30.004474

22. Tromberg BJ, Svaasand LO, Tsay T, Haskell RC. Properties of photon density waves in multiple-scattering media. *Appl Opt*. 1993;32(4):607. doi:10.1364/AO.32.000607

23. Fantini S, Franceschini MA, Gratton E. Semi-infinite-geometry boundary problem for light migration in highly scattering media: a frequency-domain study in the diffusion approximation. *J Opt Soc Am B*. 1994;11(10):2128. doi:10.1364/JOSAB.11.002128

24. Tromberg BJ, Cerussi AE, Chung S-H, Tanamai W, Durkin A. Broadband Diffuse Optical Spectroscopic Imaging. *Handb Biomed Opt*. 2011;(Chapter 9):181-190.

25. O'Sullivan TD. Long-term validation of a multi-wavelength frequency-domain diffuseoptical spectroscopy instrument. 2015.

26. Tromberg BJ, Svaasand LO, Tsay TT, Haskell RC. Properties of photon density waves in multiple-scattering media. *Appl Opt*. 1993;32(4):607-616. doi:10.1364/AO.32.000607

27. Madsen SJ, Anderson ER, Haskell RC, Tromberg BJ. Portable, High-Bandwidth Frequency-Domain Photon Migration Instrument for Tissue Spectroscopy. *Opt Lett Opt Lett*. 1994;19(23):1934-1936. doi:10.1364/OL.19.001934

28. Lee J, Kim JG, Mahon S, et al. Tissue hemoglobin monitoring of progressive central hypovolemia in humans using broadband diffuse optical spectroscopy. *J Biomed Opt*. 2008;13(December):064027. doi:10.1117/1.3041712

29. Lee J, Kim JG, Mahon SB, et al. Noninvasive optical cytochrome c oxidase redox state measurements using diffuse optical spectroscopy. *J Biomed Opt*. 2014;19(5):055001. doi:10.1117/1.jbo.19.5.055001

30. Ganesan G, Warren R V, Leproux A, et al. Diffuse optical spectroscopic imaging of subcutaneous adipose tissue metabolic changes during weight loss. *Int J Obes*. 2016;40(8):1292-1300. doi:10.1038/ijo.2016.43

31. Warren R V., Cotter J, Ganesan G, et al. Noninvasive optical imaging of resistance training adaptations in human muscle. *J Biomed Opt*. 2017;22(12):1. doi:10.1117/1.JBO.22.12.121611

32. Ueda S, Roblyer D, Cerussi A, et al. Baseline tumor oxygen saturation correlates with a pathologic complete response in breast cancer patients undergoing neoadjuvant chemotherapy. *Cancer Res*. 2012;72(17):4318-4328. doi:10.1158/0008-5472.CAN-12-0056

33. Tromberg BJ, Zhang Z, Leproux A, et al. Predicting responses to neoadjuvant chemotherapy in breast cancer: ACRIN 6691 trial of diffuse optical spectroscopic imaging. *Cancer Res*. 2016;76(20):5933-5944. doi:10.1158/0008-5472.CAN-16-0346

34. Shah N, Tromberg BJ, Hsiang D, Cerussi A, Butler J, Durkin A. In vivo absorption, scattering, and physiologic properties of 58 malignant breast tumors determined by broadband diffuse optical spectroscopy. *J Biomed Opt*. 2006;11(4):044005. doi:10.1117/1.2337546

35. Leproux A, Kim YM, Min JW, et al. Differential diagnosis of breast masses in South Korean premenopausal women using diffuse optical spectroscopic imaging. *J Biomed Opt*. 2016;21(7):74001. doi:10.1117/1.JBO.21.7.074001

36. Fishkin JB, Fantini S, vandeVen MJ, Gratton E. Gigahertz photon density waves in a turbid medium: Theory and experiments. *Phys Rev E - Stat Physics, Plasmas, Fluids, Relat Interdiscip Top*. 1996;53(3):2307-2319. doi:10.1103/PhysRevE.53.2307

37. Yodh A, Chance B. Spectroscopy and Imaging with Diffusing Light. *Phys Today*. 1995;48(3):34-40. doi:10.1063/1.881445

38. Flock ST, Patterson MS, Wilson BC, Wyman DR. Monte Carlo Modeling of Light Propagation in Highly Scattering Tissues—I: Model Predictions and Comparison with Diffusion Theory. *IEEE Trans Biomed Eng*. 1989;36(12):1162-1168.

doi:10.1109/TBME.1989.1173624

39. Carp SA, Prahl SA, Venugopalan V. Radiative transport in the delta-P[sub 1] approximation: accuracy of fluence rate and optical penetration depth predictions in turbid semi-infinite media. *J Biomed Opt*. 2004;9(3):632. doi:10.1117/1.1695412

40. Kienle A, Patterson MS. Improved solutions of the steady-state and the time-resolved diffusion equations for reflectance from a semi-infinite turbid medium. *J Opt Soc Am A*. 1997;14(1):246. doi:10.1097/MCA.0000000000000282

41. Cerussi AE, Warren R, Hill B, et al. Tissue phantoms in multicenter clinical trials for diffuse optical technologies. *Biomed Opt Express*. 2012;3(5):966-971. doi:10.1364/BOE.3.000966

42. Ayers F, Grant A, Kuo D, David J, Durkin AJ. Fabrication and characterization of silicone-based tissue phantoms with tunable optical properties in the visible and near infrared domain. *Proc SPIE*. 2008;6870. doi:10.1117/12.764969

43. Leproux A, O'Sullivan TD, Cerussi A, et al. Performance assessment of diffuse optical spectroscopic imaging instruments in a 2-year multicenter breast cancer trial. *J Biomed Opt*. 2017;22(12):1. doi:10.1117/1.JBO.22.12.121604

44. Pifferi A, Torricelli A, Taroni P, Comelli D, Bassi A, Cubeddu R. Fully automated time domain spectrometer for the absorption and scattering characterization of diffusive media. *Rev Sci Instrum*. 2007;78(5). doi:10.1063/1.2735567

45. O'Sullivan T, Leproux A, Chen J-. H, et al. Optical imaging correlates with magnetic resonance imaging breast density and reveals composition changes during neoadjuvant chemotherapy. *Breast Cancer Res*. 2013;15:1-15. doi:10.1186/bcr3389

46. Santoro Y, Leproux A, Cerussi A, Tromberg B, Gratton E. Breast cancer spatial heterogeneity in near-infrared spectra and the prediction of neoadjuvant chemotherapy response. *J Biomed Opt*. 2011;16(9):097007. doi:10.1117/1.3638135

47. Fabbri F, Sassaroli A, Henry ME, Fantini S. Optical measurements of absorption changes in two-layered diffusive media. *Phys Med Biol*. 2004;49(7):1183-1201. doi:10.1088/0031-9155/49/7/007

48. Pucci O, Toronov V, St. Lawrence K. Measurement of the optical properties of a two-layer model of the human head using broadband near-infrared spectroscopy. *Appl Opt*. 2010;49(32):6324-6332. doi:10.1364/AO.49.006324

49. Gagnon L, Cooper RJ, Yücel MA, Perdue KL, Greve DN, Boas DA. Short separation channel location impacts the performance of short channel regression in NIRS. *Neuroimage*. 2012;59(3):2518-2528. doi:10.1016/j.neuroimage.2011.08.095

50. Saager RB, Berger AJ. Direct characterization and removal of interfering absorption trends in two-layer turbid media. *J Opt Soc Am A*. 2005;22(9):1874.

doi:10.1364/josaa.22.001874

51. Pollard V, Prough DS, DeMelo AE, Deyo DJ, Uchida T, Stoddart HF. Validation in Volunteers of a Near-Infrared Spectroscope for Monitoring Brain Oxygenation In Vivo. *Anesth Analg*. 1996;82(2):269-277. doi:10.1097/00000539-199602000-00010

52. Jelzow A, Wabnitz H, Tachtsidis I, Kirilina E, Brühl R, Macdonald R. Separation of superficial and cerebral hemodynamics using a single distance time-domain NIRS measurement. *Biomed Opt Express*. 2014;5(5):1465. doi:10.1364/boe.5.001465

53. Pham TH, Spott T, Svaasand LO, Tromberg BJ. Quantifying the properties of two-layer turbid media with frequency-domain diffuse reflectance. *Appl Opt*. 2000;39(25):4733. doi:10.1364/ao.39.004733

54. Lee J, Kim JG, Mahon S, et al. Broadband diffuse optical spectroscopy assessment of hemorrhage- and hemoglobin-based blood substitute resuscitation. *J Biomed Opt*. 2010;14(4):044027. doi:10.1117/1.3200932

55. Lee J, Cerussi AE, Saltzman D, Waddington T, Tromberg BJ, Brenner M. Hemoglobin measurement patterns during noninvasive diffuse optical spectroscopy monitoring of hypovolemic shock and fluid replacement. *J Biomed Opt*. 2007;12(April):024001. doi:10.1117/1.2715189

56. Lam JH, O'Sullivan TD, Park TS, et al. Non-invasive Dual-Channel Broadband Diffuse Optical Spectroscopy of Massive Hemorrhage and Resuscitative Endovascular Balloon Occlusion of the Aorta (REBOA) in Swine. *Mil Med*. 2018;183(suppl_1):150-156. doi:10.1093/milmed/usx163

57. Franceschini MA, Boas DA, Zourabian A, et al. Near-infrared spiroximetry: noninvasive measurements of venous saturation in piglets and human subjects. *J Appl Physiol*. 2002;92(1):372-384. doi:10.1152/jappl.2002.92.1.372

58. Franceschini MA, Gratton E, Fantini S. Noninvasive optical method of measuring tissue and arterial saturation:an application to absolute pulse oximetry of the brain. *Opt Lett*. 1999;24(12):829. doi:10.1364/OL.24.000829

59. Dunn JOC, Mythen MG, Grocott MP. Physiology of oxygen transport. *BJA Educ*. 2016;16(10):341-348. doi:10.1093/bjaed/mkw012

60. Shepherd SJ, Pearse RM. Role of central and mixed venous oxygen saturation measurement in perioperative care. *Anesthesiology*. 2009;111(3):649-656. doi:10.1097/ALN.0b013e3181af59aa

61. Blockley NP, Griffeth VEM, Simon AB, Buxton RB. A review of calibrated blood oxygenation level-dependent (BOLD) methods for the measurement of task-induced changes in brain oxygen metabolism. *NMR Biomed*. 2013;26(8):987-1003. doi:10.1002/nbm.2847

62. Raichle ME, MacLeod AM, Snyder AZ, Powers WJ, Gusnard DA, Shulman GL. A

default mode of brain function. *Proc Natl Acad Sci U S A*. 2001;98(2):676-682. doi:10.1073/pnas.98.2.676

63. Dunn AK, Devor A, Dale AM, Boas DA. Spatial extent of oxygen metabolism and hemodynamic changes during functional activation of the rat somatosensory cortex. *Neuroimage*. 2005;27(2):279-290. doi:10.1016/j.neuroimage.2005.04.024

64. Boas DA, Campbell LE, Yodh AG. Scattering and Imaging with Diffusing Temporal Field Correlations. *Phys Rev Lett*. 1995;75(9):1855-1858. doi:10.1103/PhysRevLett.75.1855

65. Boas DA, Yodh AG. Spatially varying dynamical properties of turbid media probed with diffusing temporal light correlation. *J Opt Soc Am A*. 1997;14(1):192. doi:10.1364/josaa.14.000192

66. Leproux A, Durkin A, Compton M, Cerussi AE, Gratton E, Tromberg BJ. Assessing tumor contrast in radiographically dense breast tissue using Diffuse Optical Spectroscopic Imaging (DOSI). *Breast Cancer Res*. 2013;15(5). doi:10.1186/bcr3485

67. O'Sullivan TD, Cerussi AE, Cuccia DJ, Tromberg BJ. Diffuse optical imaging using spatially and temporally modulated light. *J Biomed Opt*. 2012;17(7):0713111. doi:10.1117/1.JBO.17.7.071311

68. Delpy DT, Cope M, Van Der Zee P, Arridge S, Wray S, Wyatt J. Estimation of optical pathlength through tissue from direct time of flight measurement. *Phys Med Biol*. 1988;33(12):1433-1442. doi:10.1088/0031-9155/33/12/008

69. Niehorster DC, Li L, Lappe M. The accuracy and precision of position and orientation tracking in the HTC vive virtual reality system for scientific research. *Iperception*. 2017;8(3):1-23. doi:10.1177/2041669517708205

70. Ghijsen M. Quantitative real-time optical imaging of the tissue metabolic rate of oxygen consumption. *J Biomed Opt*. 2018;23(03):1. doi:10.1117/1.jbo.23.3.036013

71. Magder S. Volume and its relationship to cardiac output and venous return. *Crit Care*. 2016;20(1):1-11. doi:10.1186/s13054-016-1438-7

72. Boas DA, Gaudette T, Strangman G, Cheng X, Marota JJA, Mandeville JB. The accuracy of near infrared spectroscopy and imaging during focal changes in cerebral hemodynamics. *Neuroimage*. 2001;13(1):76-90. doi:10.1006/nimg.2000.0674

73. Cui W, Wang N, Chance B. Study of photon migration depths with time-resolved spectroscopy. *Opt Lett*. 1991;16(21):1632. doi:10.1364/ol.16.001632

74. Weiss GH, Nossal R, Bonner RF. Statistics of penetration depth of photons re-emitted from irradiated tissue. *J Mod Opt*. 1989;36(3):349-359. doi:10.1080/09500348914550381

75. Sevick EM, Frisoli JK, Burch CL, Lakowicz JR. Localization of absorbers in scattering media by use of frequency-domain measurements of time-dependent photon migration. *Appl Opt*. 1994;33(16):3562-3570. doi:10.1364/AO.33.003562

76. Coffman JD, Gregg DE. Oxygen metabolism and oxygen debt repayment after myocardial ischemia. *Am J Physiol*. 1961;201:881-887. doi:10.1152/ajplegacy.1961.201.5.881

77. Furusawa K, Hill A V, Long CNH, Lupton H. Muscular exercise and oxygen requirement. *Roy Soc Pro*. 1924;97:167-176.

78. Amelard R, Lam JH, Hill B, Durkin A, Cutler K, Tromberg BJ. Monocular 3D Probe Tracking for Generating Sub-Surface Optical Property Maps from Diffuse Optical Spectroscopic Imaging. *IEEE Trans Biomed Eng*. 2019;PP(XX). doi:10.1109/TBME.2019.2950004

79. Morrison JJ, Ross JD, Houston R, Watson JDB, Sokol KK, Rasmussen TE. Use of resuscitative endovascular balloon occlusion of the aorta in a highly lethal model of noncompressible torso hemorrhage. *Shock*. 2014;41(2):130-137. doi:10.1097/SHK.0000000000000085

80. White JM, Cannon JW, Stannard A, Markov NP, Spencer JR, Rasmussen TE. Endovascular balloon occlusion of the aorta is superior to resuscitative thoracotomy with aortic clamping in a porcine model of hemorrhagic shock. *Surgery*. 2011;150(3):400-409. doi:10.1016/j.surg.2011.06.010

81. Park TS, Batchinsky AI, Belenkiy SM, et al. Resuscitative endovascular balloon occlusion of the aorta (REBOA): Comparison with immediate transfusion following massive hemorrhage in swine. *J Trauma Acute Care Surg*. 2015;79(6):930-936.

82. Qasim Z, Brenner M, Menaker J, Scalea T. Resuscitative endovascular balloon occlusion of the aorta. *Resuscitation*. 2015;96:275-279. doi:10.1016/j.resuscitation.2015.09.003

83. Brenner ML, Moore LJ, DuBose JJ, et al. A clinical series of resuscitative endovascular balloon occlusion of the aorta for hemorrhage control and resuscitation. *J Trauma Acute Care Surg*. 2013;75(3):506-511. doi:10.1097/TA.0b013e31829e5416

84. Markov NP, Percival TJ, Morrison JJ, et al. Physiologic tolerance of descending thoracic aortic balloon occlusion in a swine model of hemorrhagic shock. *Surg (United States)*. 2013;153(6):848-856. doi:10.1016/j.surg.2012.12.001

85. Avaro J-P, Mardelle V, Roch A, et al. Forty-Minute Endovascular Aortic Occlusion Increases Survival in an Experimental Model of Uncontrolled Hemorrhagic Shock Caused by Abdominal Trauma. *J Trauma Inj Infect Crit Care*. 2011;71(3):720-726.

86. Ledgerwood A, Kazmers M, Lucas C. The Role of Thoracic Aortic Occlusion for Massive Hemoperitoneum. *J Trauma*. 1976;16(8):610-615. doi:10.1097/00005373-197608000-00004

87. Stannard A, Eliason JL, Rasmussen TE. Resuscitative Endovascular Balloon Occlusion of the Aorta (REBOA) as an Adjunct for Hemorrhagic Shock. *J Trauma Inj Infect Crit Care*. 2011;71(6):1869-1872. doi:10.1097/TA.0b013e31823fe90c

88. Cerussi A, Shah N, Hsiang D, Durkin A, Butler J, Tromberg BJ. In vivo absorption, scattering, and physiologic properties of 58 malignant breast tumors determined by broadband diffuse optical spectroscopy. *J Biomed Opt*. 2006;11(4). doi:10.1117/1.2337546

89. Schmitt JM, Kumar G. Optical scattering properties of soft tissue: a discrete particle model. *Appl Opt*. 1998;37(13):2788-2797. doi:10.1364/AO.37.002788

90. Jakubowski D. Development of Broadband Quantitative Tissue Optical Spectroscopy for the Non-Invasive Characterization of Breast Disease. 2002. http://search.proquest.com/docview/304798175?accountid=14509.

91. Russo RM, Williams TK, Grayson JK, et al. Extending the golden hour: Partial resuscitative endovascular balloon occlusion of the aorta in a highly lethal swine liver injury model. *J Trauma Acute Care Surg*. 2016;80(3):372-380. doi:10.1097/TA.0000000000000940

92. Yu G, Durduran T, Zhou C, Cheng R, Yodh A. Near-Infrared Diffuse Correlation Spectroscopy for Assessment of Tissue Blood Flow. In: *Handbook of Biomedical Optics*. CRC Press; 2011:195-216. doi:doi:10.1201/b10951-13

93. Yazdi SS. A Fully Integrated Frequency-Domain Diffuse Optical Imaging System in 180 nm Standard CMOS. 2017.

94. Sthalekar CC, Miao Y, Koomson VJ. Optical Characterization of Tissue Phantoms Using a Silicon Integrated fdNIRS System on Chip. *IEEE Trans Biomed Circuits Syst*. 2017;11(2):279-286. doi:10.1109/TBCAS.2016.2586103

95. Lee M, June S, Kim S. Developing a compact multiple laser diode combiner with a single fiber stub output for handheld IoT devices. *J Korean Phys Soc*. 2018;72(1):71-78. doi:10.3938/jkps.72.71

APPENDIX: Diagrams and data used to optimize the high-speed, multi-modal DOSI platform

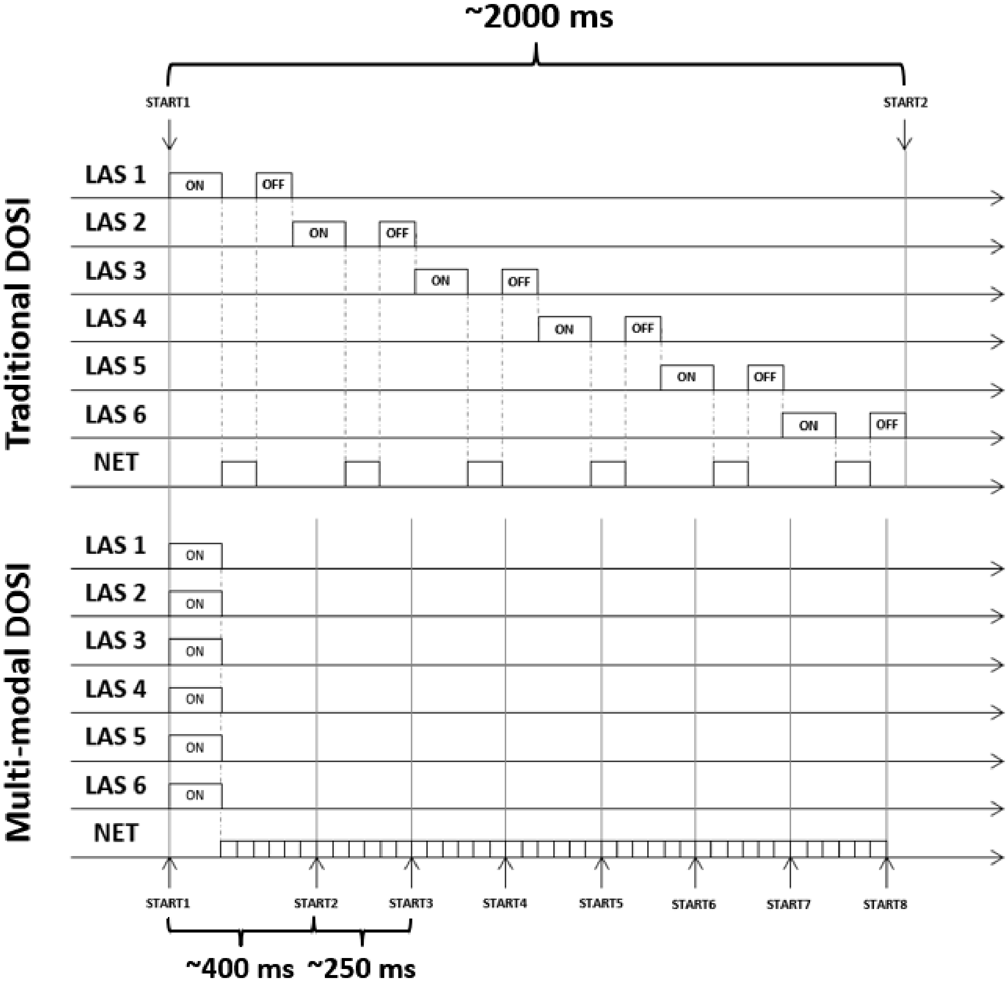

Figure 30: Relative system timing diagram comparing the old timing scheme to the new timing scheme for the multi-modal DOSI system. LAS # refers to a laser diode in the system, and NET refers to network analyzer activity. Each solid vertical line refers to the start of a new measurement. (top) Previously used timing scheme for the multi-modal DOSI system running the 6-wavelength DOSI system at ~0.5 Hz. Each laser is turned on during a NET frequency sweep, and turned off once the frequency sweep is completed. (bottom) New timing scheme which maintains all of the lasers on. Frequency sweeping is still applied sequentially to laser diodes. For a 6-wavelength system, an instrument acquisition rate of ~4 Hz was estimated.

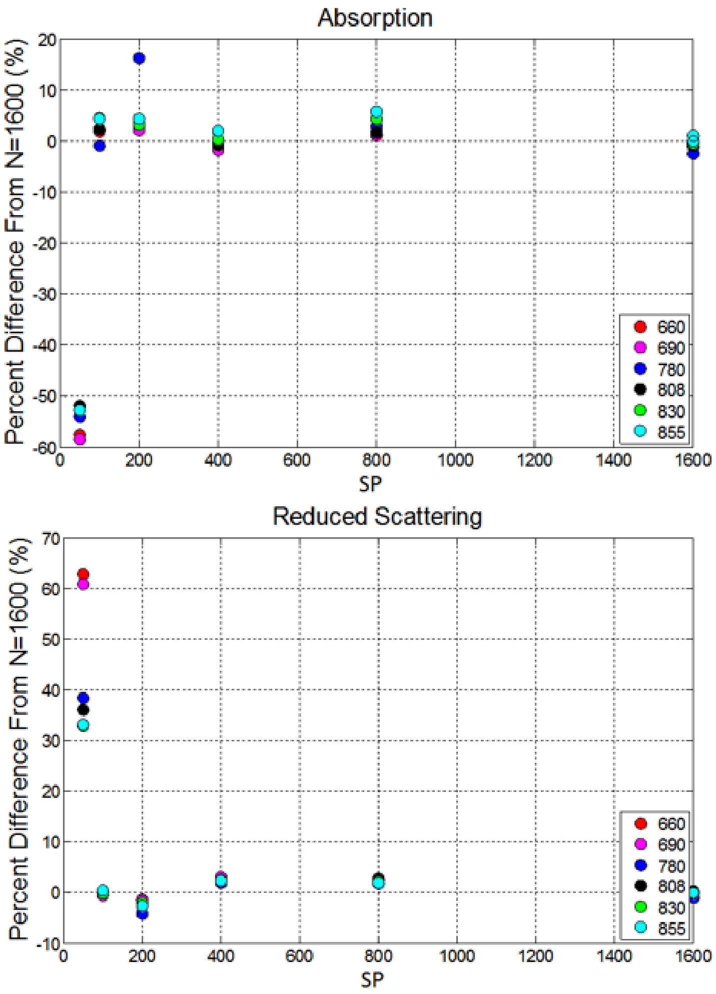

Figure 31: Experiment to determine the minimum useable sampling points (SP) without sacrificing system accuracy. A set of three measurements were performed on a phantom using a frequency sweep with the interval 50-500 MHz and then repeated with reducing SP. Optical properties of the data at each SP interval was examined, and the percent difference compared to a separate measurement set using 1600 SP was calculated. With the exception of a single laser diode for a single measurement, optical properties for absorption and reduced scattering at 151 SP remained well within 10% of optical properties reported at 1600 SP. Thus, SP should be selected at least 0.335 points/MHz.

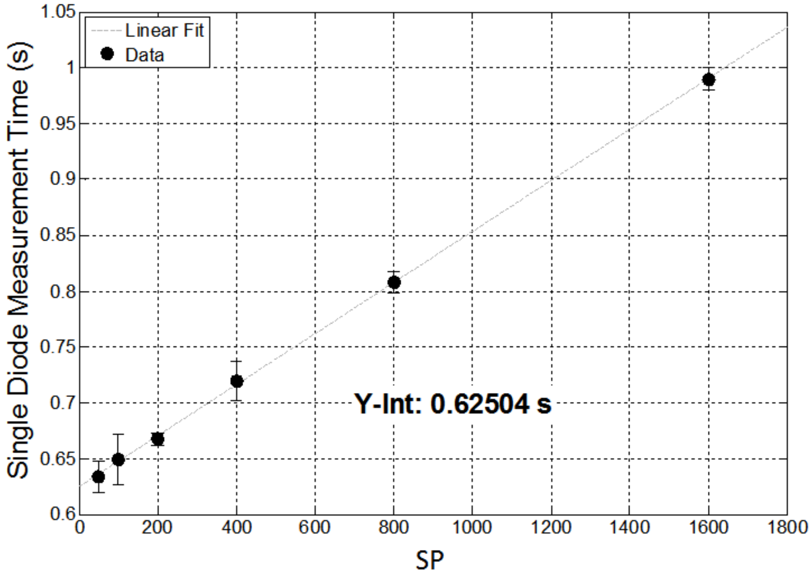

Figure 32: System acquisition speed as a function of network analyzer sampling points (SP). The data was fit using a first-order polynomial in order to estimate the 0 SP time. From the data, it was determined that reducing the SP from 400 to ~151 would reduce the measurement time by ~70 ms per laser diode. This time reduction is not insignificant, potentially affecting a six-laser diode system by ~400ms. It can also be extrapolated from the data that even at 0 SP, the laser diode dwell time is ~625ms, which is the speed bottleneck due to other components in the system.